- 1 A multi-region neural interface for analgesic delivery
- Guanghao Sun^{1,2,3}, Fei Zeng², Michael McCartin², Qiaosheng Zhang^{2,3}, Helen Xu², Yaling Liu², 3
- Zhe Sage Chen^{1,3,4,5,*}, Jing Wang^{2,3,4,5}* 4

6

2

5

- 1. Department of Psychiatry, New York University Grossman School of Medicine, New York, NY
- 7 10016, USA
- 8 2. Department of Anesthesiology, Perioperative Care and Pain Medicine, New York University
- 9 Grossman School of Medicine, New York, NY 10016, USA
- 10 3. Interdisciplinary Pain Research Program, New York University Langone Health, New York,
- 11 NY 10016, USA
- 12 4. Department of Neuroscience & Physiology, New York University Grossman School of
- 13 Medicine, New York, NY 10016, USA
- 14 5. Neuroscience Institute, New York University Grossman School of Medicine, New York, NY
- 10016, USA 15

18

- 16 Correspondence: *Equal contribution by <u>zhe.chen@nyulangone.org</u> (ZSC) and
- 17 jing.wang2@nyulangone.org (JW)

20 **One sentence summary** (< 150 characters):

- A multi-region brain machine interface automatically detects pain with high accuracy and
- delivers ultrafast analgesia for acute and chronic pain.

ABSTRACT

24

25

26

27

28

29

30

31

32

33

34

35

36

37

38

39

40

41

Effective treatments for chronic pain remain limited. Conceptually, a closed-loop neural interface combining sensory signal detection with therapeutic delivery can produce timely and effective pain relief. Such systems are challenging to develop due to difficulties in accurate pain detection and ultrafast analgesic delivery. Pain has sensory and affective components, encoded in large part by neural activities in the primary somatosensory cortex (S1) and anterior cingulate cortex (ACC), respectively. Meanwhile, studies show that stimulation of the prefrontal cortex (PFC) produces descending pain control. Here, we have designed a brain-machine interface (BMI) combining an automated pain detection arm, based on simultaneously recorded local field potential (LFP) signals from the S1 and ACC, with a treatment arm, based on optogenetic activation or electrical deep brain stimulation (DBS) of the PFC in freely behaving rats. Our multi-region neural interface accurately detected and treated acute evoked pain and, more importantly, spontaneous pain associated with chronic pain. This neural interface performed with minimal delay and remained stable over time. Given the clinical feasibility of LFP recordings and DBS, our findings demonstrate the promising potential of BMIs for pain treatment.

INTRODUCTION

Closed-loop brain-machine interfaces (BMIs) link neural signals for a sensory or motor event with neuromodulation and have the potential to treat neuropsychiatric disorders(1-3). BMIs have produced promising results for treating epilepsy and motor neuron diseases(4-8). However, their application to sensory disorders have been limited by challenges in detecting accurate sensory signals and providing fast and effective behavioral feedback.

Pain represents a unique challenge as well as an opportunity for BMI designs. Chronic pain is one of the most common sensory disorders, and it is defined by discrete episodes of pain that either are evoked by noxious stimuli or occur spontaneously(9). Current treatments are limited to scheduled pharmacological interventions and continuous spinal neuromodulation. These therapeutic options do not take into consideration the precise timing of individual pain episodes, resulting in frequent treatment delays and under- or overtreatment(10). Conceptually, a BMI approach is ideally suited to pain management by selectively targeting discrete nociceptive episodes. However, decoding pain signals remains challenging. Unlike other sensory modalities(11), there is no single target for pain representations(12-16). Among a distributed network of pain-processing regions, the primary somatosensory cortex (S1) is known to encode sensory-discriminative aspect of pain, including the location, timing, and quality of pain, whereas the anterior cingulate cortex (ACC) is known to play a key role in aversive response to pain(12-14, 17-20). Thus, an appealing strategy to decode pain is to integrate neural signals from multiple regions, with the S1 and ACC as the most relevant targets.

Current BMI applications primarily rely on neuronal spikes to produce accurately decoded signals. 64 65 However, individual spikes are difficult to record faithfully over a prolonged period of time, which 66 is needed for the management of chronic pain. In contrast, local field potentials (LFPs), which represent the subthreshold synaptic activity from local neuronal populations(21, 22), are relatively 67 68 stable in chronic recordings. Although their signal stability facilitates clinical applications, LFPs 69 have only recently started to be used for population decoding for BMI applications (23-25). 70 71 In terms of treatment targets, the prefrontal cortex (PFC) is an important center for top-down 72 control of sensory experiences (26). Human and animal studies have shown that decreased activity in the PFC contributes to symptoms of chronic pain(27-32). Importantly, stimulation of excitatory 73 74 neurons in the PFC can produce rapid inhibition of withdrawal reflexes and aversive responses to 75 pain without substantial side effects(32-37), supporting the use of PFC as a potential therapeutic 76 arm in BMI design. 77 In this study, we have developed an LFP-based decoding strategy using recordings from rodent S1 78 79 and ACC, and combined it with optogenetic or electrical stimulation of the PFC to form a multi-80 region neural interface. We show that this neural interface can deliver analgesia with high 81 sensitivity and specificity over a long period of time. 82 83 **RESULTS**

Design of a stable multi-region neural interface to detect and treat pain in real time

The S1 is known to provide sensory information for noxious inputs(16). Previous studies have

shown that neural spikes from this region may decode the onset of pain that is generated in the

84

85

corresponding somatotopic area(38, 39). Meanwhile, studies indicate that the ACC, particularly the rostral ACC, regulates the affective component of pain and can be used to decode both the onset and intensity of pain(12, 13, 19, 39). At the same time, stimulation of the prelimbic PFC (PL-PFC) has been shown to activate top-down regulatory pathways to inhibit pain(32-37). Based on these studies, we developed a multi-region, closed-loop neural interface for nociceptive control by using a pain decoder based on concurrent neural signals from the ACC and S1 to trigger therapeutic stimulation of the PL-PFC in freely behaving rats (Fig. 1, A and B, and figs. S1 and S2). To decode pain onset, we recorded LFPs (21, 22), which are known to remain stable in chronic electrophysiological recordings (23-25). Here, we recorded LFPs simultaneously from the rostral ACC and the hind limb region of S1 (fig. S3A), while stimulating the contralateral hind paw of rats with either noxious pin pricks (PP) or non-noxious von Frey filaments (vF). From these neural signals, we could readily identify pain-evoked event-related potentials (ERPs) from the ACC and S1 (fig. S3A), indicating that nociceptive signals are contained within these two regions (12-14, 17-20). We extracted the ERP latency on a trial-by-trial basis (see Supplementary Materials and Methods), and found that the ERP peak latency in the ACC was on average slightly longer than the latency in the S1, suggesting that nociceptive information arrived at the S1 before the ACC (fig. S3B), compatible with earlier reports(40-42). These results support the use of LFP signals from S1 and ACC to decode pain.

105

106

107

108

109

87

88

89

90

91

92

93

94

95

96

97

98

99

100

101

102

103

104

We designed a model-based unsupervised learning approach to decode pain from multi-region LFP signals. Prior work has shown that spectral features from low gamma (30-50 Hz), high gamma (50-100 Hz), and ultra-high frequency (300-500 Hz) bands are particularly relevant for cortical pain processing(41-43). The ultra-high frequency power can be viewed as a proxy for multiunit

activity (MUA). Thus, we computed frequency-dependent LFP power features and inputted these features into a real-time neural decoder based on a state space model (SSM) (Fig. 1, C to E; Supplementary Materials and Methods). In the presence of a noxious stimulus, the SSM identified a relative change in observed neural activity (Z-scored) from the baseline, and used this change in activity as a proxy for the acute pain signal. To optimize the specificity of pain detection, we designed a cross-correlation function (CCF, see Supplementary Materials and Methods) to track temporally coherent changes of pain-encoded LFP features in the S1 and ACC, as the use of concurrent signals from these cortical regions allowed us to capture both sensory and aversive components of pain(12-14, 17-20). This CCF combined the two SSM-inferred Z-scores derived separately from the ACC and S1 LFP features, and optimized the detection performance by adjusting the relative weights of each region's contributions. For online BMI experiments, we used the CCF-based decoder to automatically detect the onset of nociceptive signal to trigger optogenetic or electrical stimulation of the PL-PFC to control pain (Fig. 1, A and B, and figs. S1 and S2).

We tested our decoding strategy in a set of pain assays. First, we delivered a noxious PP or non-noxious 2g or 6g vF stimulus to the rat's hind paw, while recording LFPs from the contralateral areas of the rostral ACC and the hind limb region of the S1 (Fig. 2A). As expected, rats showed a higher paw withdrawal rate in response to PP than to vF stimulations (Fig. 2B). In online experiments, our SSM decoder successfully detected the onset of noxious PP stimulus (Fig. 2C), as opposed to non-noxious vF stimulus (Fig. 2D). Using this method, we trained the decoder with a few calibration trials with PP and conducted online BMI behavior experiments that continuously and automatically detected the onset of pain signals (Fig. 2E). The detection rate for the noxious

stimulus (PP) was higher than the non-noxious stimulus (2g or 6g vF) based on LFPs from ACC, S1 or a combination of ACC and S1 (the CCF method) (Fig. 2F). These results suggest that our decoding paradigm can detect "painful" stimuli and distinguish them from "non-painful" stimuli of varying intensities. The area under curve (AUC, see Supplementary Materials and Methods) was computed to further validate the detection accuracy of the system (Table S1). The results show that AUC values for detecting 2g vF or 6g vF are both at chance accuracy; in contrast, the AUC value for detecting PP is higher. In addition, detection using the CCF method is superior to decoding using either the ACC or S1 alone (Fig. 2F, Table S1). To further quantify the accuracy of the CCF-based decoding method, we compared the false detection rate produced by the CCF strategy with the false detection rate produced by single-region decoding methods. We found that the multi-region decoding strategy showed a substantial reduction in false detections (Fig. 2G), likely contributing to the enhanced specificity of CCF-based decoding. Such high true detection and low false detection rates are critical for a real-world implementation of a BMI system and demonstrates the importance of using multiple regions to optimize pain decoding.

For therapeutic BMI applications, signal stability is critical. We tested the reliability of the LFP signals and found that our LFP-based decoding strategy maintained a high degree of accuracy over three months (Fig. 2H, fig. S4A). Furthermore, when we used the model parameters derived from day 1 of testing, we found that the same model was able to detect pain with high accuracy on day 5, suggesting that the model parameters may not require frequent training or calibration (Fig. 2I, fig. S4B). Such signal and model fidelity for pain decoding are appealing for real-world applications with chronic neural recordings.

Automated pain detection and analgesic delivery by the multi-region neural interface

156

157 Having established the accuracy, specificity, and reliability of our CCF-based pain decoder, we 158 coupled this decoder with optogenetic stimulation of pyramidal neurons of the PL-PFC (using a 159 CaMKII promotor to express channelrhodopsin (ChR2)) to form an analgesic BMI (Fig. 1, A and 160 B, and figs. S1 and S2). We used a conditioned place preference (CPP) assay to assess how this 161 BMI could inhibit acute mechanical pain(19, 37, 40). In the preconditioning phase, animals moved 162 freely between two chambers. During conditioning, we paired each chamber with a peripheral 163 (noxious or non-noxious) stimulus in combination with BMI or various control optogenetic 164 neurostimulation protocols (Fig. 3A). In the testing phase, we removed peripheral stimuli and 165 neurostimulation and allowed the rats to move freely again. If the BMI treated pain, rats should 166 prefer the chamber associated with the BMI during the testing phase. A CPP score was calculated 167 by subtracting the time rats spent in the BMI-paired chamber during the preconditioning phase 168 from the time they spent in the testing phase, to quantify the effects of BMI on reducing pain-169 aversion. First, we compared noxious PP stimulation coupled with BMI-triggered optogenetic 170 stimulation of the PL-PFC (BMI + PP) against PP coupled with random PL-PFC stimulation of 171 matching duration and intensity (random neurostimulation + PP). Rats preferred the chamber 172 associated with the BMI, suggesting that it reduced acute mechanical pain (Fig. 3B). We then 173 repeated this experiment on rats that expressed yellow fluorescent protein (YFP), and found that 174 YFP-treated control rats did not experience pain relief (fig. S5A). A comparison of the CPP scores 175 highlighted the efficacy of the BMI in delivering analgesia (Fig. 3B). As a positive control, we 176 compared manual activation of the PL-PFC directly following delivery of PP to the paw (manual 177 + PP) against random PL-PFC stimulation coupled with PP (random + PP). Here, we observed a 178 preference for manual PL-PFC activation in ChR2 rats but not YFP rats (Fig. 3C and fig. S5B),

compatible with earlier reports (*33*, *37*). Results from Figs. 3B and 3C suggest the BMI worked as well as precise manual control of the PL-PFC. To confirm this finding, we compared BMI control of the PL-PFC in the presence of PP with manual control of PL-PFC in the presence of PP, and found that rats could not distinguish between the two treatments (Fig. 3D and fig. S5C). Finally, to demonstrate that the effects of the PL-PFC activation delivered by the BMI were specific to pain, we examined the rats' preference for BMI in the presence of a non-noxious vF stimulus (by comparing BMI + 6g vF with random PL-PFC activation + 6g vF), and found that rats did not show a preference for either chamber (Fig. 3E and fig. S5D). These results support the specificity of the BMI in delivering pain control without substantial side effects. Furthermore, we found that BMI treatment also reduced firing rates of ACC neurons in response to noxious stimuli (fig. S6).

We then tested this multi-region BMI on acute thermal pain using a Hargreaves test. We first delivered infrared (IR) stimulations at two different intensities – noxious IR 70 and non-noxious IR 10 – to the rats' hind paws (Fig. 4A). Rats withdrew their paws 100% of the time with IR 70 stimulations, compared to <10% of the time with IR 10 stimulations (Fig. 4B). Our multi-region LFP-based pain decoder successfully detected the onset of thermal pain before paw withdrawals in response to noxious stimulation (Fig. 4C), but not to non-noxious thermal stimulation (Fig. 4D). Similar to the decoding of mechanical pain, CCF-based pain decoding showed a lower (<10%) false positive detection rate than single-region decoding, while maintaining high (~80%) detection rate for noxious stimulations. This remained true even when non-noxious stimulations of varying intensities (IR 10 and 20) were administered, demonstrating the ability of the decoder to specifically distinguish pain episodes rather than different stimulus intensities (Fig. 4E, Table S2). Next, we tested the efficacy of this BMI in relieving thermal pain (fig. S7). We found the latency

to paw withdrawal increased in the presence of neurostimulation driven by the multi-region BMI, and that the BMI achieved similar effects in reducing withdrawals as manually controlled constitutive PL-PFC activation (Fig. 4F). As expected, control rats that expressed YFP did not demonstrate pain relief (Fig. 4G).

Closed-loop multi-region neural interface inhibits inflammatory pain

Next, we tested whether this closed-loop multi-region neural interface can also treat chronic pain, using a well-known inflammatory pain model – Complete Freund's Adjuvant (CFA) model. We injected CFA into the rats' paws contralateral to the implanted recording electrodes (Fig. 5A, see Supplementary Materials and Methods). CFA-treated rats demonstrated persistent mechanical allodynia lasting 14 days (Fig. 5B), and showed higher rates of paw withdrawal in response to 6g vF (allodynia-inducing) stimulations than 0.4g vF (non-allodynic) stimulations (Fig. 5C). Our LFP-based decoding strategy reliably detected the onset of allodynic episodes (Fig. 5D). Again, the CCF method produced a lower rate of false detections, while maintaining relatively high decoding sensitivity (Fig. 5E, Table S2). Furthermore, we found that application of this BMI reduced mechanical allodynia in CFA-treated rats (Fig. 5F).

Next, we tested the anti-aversive effects of BMI in the CFA model using the CPP assay (Fig. 6A). We paired the allodynic 6g vF stimulus with the BMI in one chamber and with random PL-PFC activation of matching duration and intensity in the opposite chamber. Rats expressing ChR2 showed a preference for the BMI-paired chamber (Fig. 6B); YFP rats, in contrast, did not show any chamber preference (Fig. 6C and fig. S8A). To ensure that the anti-aversive effects of this BMI were specific to pain, we repeated the same experiments using a non-allodynic 0.4 g vF

stimulus. In this case, neither ChR2 rats nor YFP rats showed any preference for the BMI treatment (Fig. 6, D and E, and fig. S8B).

227

228

229

230

231

232

233

234

235

236

237

238

239

240

241

242

243

244

225

226

In addition to hypersensitivity to evoked stimulus, a key pathologic feature of chronic pain is tonic, or spontaneously occurring, pain. Currently, no assays can reliably identify the onset of these spontaneous pain episodes, rendering the timing of treatment exceedingly difficult, which results in either delayed, under- or overtreatment. We used a classic CPP to unmask tonic pain in CFAtreated rats(33, 44, 45). In this assay, one of the chambers was paired with our multi-region BMI, and the other chamber was paired with random PL-PFC optogenetic stimulation. No peripheral stimuli were given, but the rats were conditioned for a prolonged period of time to unmask tonic pain episodes (Fig. 6F). We trained our multi-region decoder using noxious stimulations (PP), and then allowed the trained decoder to automatically detect tonic pain events in the absence of a peripheral stimulus (Fig. 6G). During conditioning, we paired one chamber with our BMI which used automated tonic pain detection to trigger optogenetic PL-PFC activation, and the other chamber with random PL-PFC stimulation. We found that after conditioning, CFA-treated rats preferred the chamber associated with the BMI, indicating that this treatment had a high likelihood of targeting tonic pain episodes, as opposed to random PL-PFC stimulations (Fig. 6H). YFPtreated control rats did not demonstrate this preference (fig. S8C). CPP scores further quantified the efficacy of BMI in reducing the aversive response to tonic pain (Fig. 6I). These results strongly suggest that our multi-region neural interface could identify and treat spontaneous pain in a timely fashion.

246

247

245

Closed-loop deep brain stimulation delivers on-demand analgesia

While the use of optogenetics provides cell-type specific stimulation, it is not currently available for clinical application. To advance the translational value of our BMI, we replaced optogenetic stimulation of the PL-PFC with electrical deep brain stimulation (DBS), which has been safely implemented for human use(46-51). We combined electrical stimulation of the PL-PFC with the multi-region LFP-based decoder to produce a closed-loop BMI-triggered DBS system (Fig. 7A and fig. S9). First, we performed CPP to assess the efficacy of this system in treating acute mechanical pain (Fig. 7, B and C). We found that when presented with repeated noxious stimuli (PP), rats preferred the BMI-paired chamber to the chamber paired with randomly timed DBS, suggesting that BMI-triggered DBS inhibited mechanical pain (Fig. 7D). Furthermore, this BMI reduced acute thermal pain on the Hargreaves test (Fig. 7E). Next, we assessed the efficacy of this BMI-triggered DBS system in treating chronic pain. We found that our system reduced mechanical allodynia in CFA-treated rats (Fig. 7F). We then conducted CPP in the presence of an allodyniainducing stimulus (6g vF) (Fig. 7G). We found that when presented with allodynic stimuli, CFAtreated rats preferred the BMI-paired chamber, suggesting that the neural interface reduced pain aversion (Fig. 7H). Finally, we conducted the CPP assay for spontaneous pain (Fig. 7I). We trained our multi-region decoder using the allodynic 6g vF stimulus, and then allowed the decoder to automatically detect tonic pain episodes and trigger therapeutic DBS during conditioning. We found that after conditioning, CFA-treated rats preferred the BMI-paired chamber to the chamber paired with randomly delivered DBS (Fig. 7J). Likewise, when we compared conditioning with BMI-triggered DBS vs no DBS, we found that CFA-treated rats preferred the BMI-paired chamber (fig. S10, A and B). These results suggest that BMI-triggered DBS can inhibit tonic pain. To ensure that this BMI produces no gross side effects, we examined stimulation effects on locomotion and found that it had none (fig. S10C).

248

249

250

251

252

253

254

255

256

257

258

259

260

261

262

263

264

265

266

267

268

269

Closed-loop BMI inhibits chronic neuropathic pain

To further validate the efficacy of our closed-loop multi-region neural interface for delivering analgesia, we tested it with a model of chronic neuropathic pain - the Spared Nerve Injury (SNI) model (Fig. 8A, see **Supplementary Materials and Methods**) (*52*). SNI produced persistent mechanical allodynia (Fig. 8B), but allodynia was inhibited by the application of the BMI (Fig. 8C). In a CPP assay, one chamber was paired with the BMI, and the other chamber was paired with random PL-PFC electric stimulation of the same quantity and duration. No peripheral stimuli were administered, but rats were conditioned for a prolonged period of time to unmask tonic pain episodes (Fig. 8D). The decoder was trained using an allodynia-inducing stimulus (6.0g vF), and then allowed to automatically detect tonic pain events. We found that after conditioning, SNI-treated rats preferred the BMI-paired chamber (Fig. 8E). These results in chronic neuropathic pain further validate our findings in the inflammatory pain model.

DISCUSSION

In this study, we have engineered a multi-region LFP-based neural interface to deliver pain relief. Our system uses recordings from multiple brain regions to enhance the coding specificity; it is stable over time and compatible with current electroencephalographic (EEG) or electrocorticographic (ECoG) data. This interface can produce almost instantaneous pain relief. While the use of this interface with optogenetic stimulation of pyramidal PL-PFC neurons supports cell-type specificity to enable mechanistic inquiries, its success with DBS opens the possibility for clinical application.

There is not one single brain region that specifically processes pain information. Instead, different regions process different aspects of pain. To meet the challenge of accurate pain detection, we utilized a strategy that adapts to the unique multidimensional nature of the pain experience. We decoded pain based on neural signals simultaneously recorded from two different brain regions. Ascending nociceptive signals from the periphery are known to terminate in the ACC and S1. The ACC is well-known for processing the affective component of pain (12-15, 19, 38, 48, 53-57), and neural activity in this region has been previously used to decode the intensity and timing of pain(19, 38, 40, 53). The S1, meanwhile, provides critical sensory information for pain in a somatotopic manner. Prior studies have further demonstrated that information flow between these two brain regions integrates sensory and affective information to give rise to the overall pain experience (40, 41). In our study, the success of the multi-region neural interface in treating acute and chronic pain demonstrates the specificity of decoding based on concurrent signals from the S1 and ACC. Dualregion decoding improves the specificity of pain detection, compared with previous studies that relied on single-region decoding (38, 58). Mechanistically, these results also confirm that these two regions together contribute to the experience of pain.

309

310

311

312

313

314

315

316

294

295

296

297

298

299

300

301

302

303

304

305

306

307

308

Another key advance of our study is the use of LFPs to decode pain in real time. While spikes provide specific signals at the level of individual neurons, they are less stable over long time periods in freely behaving animals and in humans. LFPs provide an alternative solution for neural readout(59, 60). In our study, we were able to reliably record LFPs over a period of three months. This signal stability supports the use of LFPs for BMI applications in chronic recording conditions, which is crucial for the management of chronic pain and similar neuropsychiatric diseases. Our decoding model remains stable for five days post-training. The robustness of our model likely

results from a combination of signal stability and the use of multi-region decoding, and it shows promise for clinical translation. Future studies, however, will show if such robustness could last even longer.

A number of studies have shown that the PL-PFC provides pain inhibition through top-down projections as well as projections to other cortical areas(32-36). We have chosen this region as the therapeutic arm of our neural interface, as it is one of the few neural structures that can regulate both sensory and affective components of pain, especially in the context of nociceptive inputs. The success of our BMI in inhibiting both sensory withdrawal and pain aversion validates this choice. There is functional homology between the rodent PL-PFC and the dorsolateral PFC in primates(61, 62), and thus our neural interface may be adapted to the dorsolateral PFC to provide demand-based treatment in chronic pain patients. Mechanistically, we found that optogenetic stimulation of the pyramidal neurons in the PL-PFC reduces pain, compatible with previous results(33, 34, 36, 37, 63). In contrast, activation of inhibitory neurons in this region is known to enhance pain(32, 64). DBS does not directly target specific classes of neurons; however, at lower frequencies such as in the case of our study, it has been shown to enhance cortical outputs (65).

False detections still occur in our study, and they are likely caused by the non-specificity of neuronal firings in the S1 and ACC, and/or by the non-stationarity of neural signals in freely behaving rats. We have shown that we can minimize false detections and improve specificity by integrating neural activities from two distinct brain regions that have complementary roles in pain processing. This approach supports the multidimensional nature of the pain experience. Each cortical region may process a unique aspect of pain, in addition to other behavioral functions.

During a pain episode, however, multiple brain regions must activate/inactivate at the same time, and thus a decoder based on activities across multiple nodes of the pain network has a higher likelihood of improving specificity. This decoding approach can be extended to incorporate additional brain structures, such as the insular cortex, to further improve decoding specificity(66). In future studies, neural signals can also be combined with real-time behavioral analyses(67) to achieve even more sensitive and specific pain detection.

The PFC has multiple functions. Thus, nonspecific effects can be expected with neuromodulation treatments deployed by PFC stimulation. Nonspecific side effects are a general issue for neuromodulation, and indeed, they have been observed with existing clinical applications of DBS(68, 69). There are two strategies to reduce non-specific effects: target highly pain-specific neural structure or neuron groups, or limit treatments to a defined period of time. Currently, there is not a single known target in the central nervous system that can reliably treat pain without any side effects. In this study, we have taken up the second strategy: our closed-loop, demand-based paradigm reduces side effects by restricting neuromodulation to the duration of the detected pain episodes, and as a result, we did not observe gross behavioral deficits. Future discoveries of neuronal populations with specific pain-regulatory functions may be adapted to our therapeutic interface to further improve treatment specificity. At the same time, our BMI can also be used to facilitate such discoveries.

In our study, we have tested our therapeutic BMI for acute mechanical and thermal pain, as well as inflammatory and chronic neuropathic pain. The use of multiple preclinical pain models validates our treatment approach, and more importantly it provides a basis for human translational

studies. For example, persistent localized inflammation and peripheral neuropathy are common causes of chronic pain in patients. The success of our system in these pain models also indicates that acute and chronic pain share certain mechanistic principles in cortical processing. LFP signals can be recorded from the brains of patients who undergo stereotaxic surgeries, as in the case of the mapping of epileptic foci, and DBS is an approved method for treating brain disorders. Thus, future work shall aim to translate our findings here to human studies to test the robustness of pain detection using cortical signals and to verify that a BMI can deliver adequate treatment. Such experiments can pave the way for closed-loop treatment for pain patients.

Limitations of our work include false detection rates as discussed above and the feasibility for clinical applications of our system in its current form. While ECoG probes may be used to derive similar decoding results, further improvement of hardware design to enable a closed-loop system of decoding and stimulation is needed. In addition, refinement on the portability of our BMI system can further enable clinical application.

In conclusion, we have designed and tested a multi-region neural interface that produces reliable detection and treatment of pain. The use of LFP signals allows our pain decoder to be compatible with ECoG or even EEG recordings. Given the clinical feasibility of EEG or ECoG recordings and DBS, adaptation of our technology can thus open new doors for treatment for patients who suffer from chronic debilitating pain.

MATERIALS AND METHODS

385 Study design

The purpose of this study was to develop and test the performance of a closed-loop neural interface for pain. We hypothesized that our BMI could accurately detect acute pain episodes based on neural activity in the rodent cortex and modulate cortical areas to inhibit pain. Acute pain tests included thermal stimulations using the Hargreaves' table and mechanical stimulations using pinprick and von Frey filaments. Mechanical stimulations were repeated on models of chronic inflammatory and neuropathic pain conditions modeled by CFA and SNI, respectively. Pain decoding was achieved through unsupervised machine learning of LFP data recorded from surgically implanted silicon probes in the S1 and ACC. Pain inhibition was achieved by optogenetic or deep brain stimulation of the PL-PFC and assessed by Hargreaves' test, mechanical allodynia and CPA or CPP. In each pain experiment, the performance of the BMI system was compared with random or manually controlled stimulations or no stimulations as control. Sample size was informed by previous similar studies. Behavioral and neural data for each of our experiments were collected from N = 10 rats for optogenetic studies (5 ChR2 rats in treatment group and 5 YFP rats in control group), and N = 12 rats for DBS studies (7 rats in CFA group and 5 rats in SNI group). Multiple experimenters in the laboratory participated in the experiment. One experimenter performed surgeries and randomly selected the treatment and control groups. Other experimenters blinded to the treatment conditions performed behavior experiments. No data was excluded.

404

405

406

407

408

386

387

388

389

390

391

392

393

394

395

396

397

398

399

400

401

402

403

Statistical analysis

Neural and behavioral data were analyzed offline through custom MATLAB (2018 version, MathWorks) scripts and GraphPad Prism version 8 software (GraphPad). Results were reported and analyzed as mean ± SEM. Comparison between mean values of two groups were evaluated

by two-tailed paired t-test, two-tailed unpaired t-test, and two-tailed Wilcoxon test. A one-way ANOVA with repeated measurements and post-hoc multiple pair-wise comparison Tukey's tests was used to compare the mean differences of more than two groups. Differences were considered to be statistically significant when P < 0.05. Exact P values and sample sizes are shown in figure legends.

ACKNOWLEDGEMENTS

Funding: This work was supported by NIH grants R01-GM115384 (J.W.), R01-NS121776 (J.W., Z.S.C.) and NSF grant CBET-1835000 (Z.S.C., J.W.). **Author contributions:** J.W. and Z.S.C. conceived, designed and supervised the study; G.S. and Q.Z. performed the surgeries and implemented the BMI hardware system. G.S., F.Z., M.M.,H.X., and Y.L. collected the data; G.S., Q.Z., Z.S.C. and J.W. developed the BMI software and analyzed data; J.W. and Z.S.C. wrote the manuscript with inputs from other authors. **Competing interests:** J.W. and Z.S.C. have applied for a patent based on this work. The other authors declare no competing interests. **Data and materials availability:** All data associated with this study are present in the paper or in the

Supplementary Materials:

Supplementary Materials.

- 428 Materials & Methods
- Fig. S1. Histology showing viral expression, and optic fiber and silicon probe implantations.
- 430 Fig. S2. Schematic of software design for a closed-loop multi-region LFP-based BMI.
- 431 Fig. S3. Pain-evoked event-related potentials (ERPs) analysis.

- 432 Fig. S4. False detection rate analysis.
- Fig. S5. LFP-based BMI does not alter pain-aversive behaviors in YFP-treated (control) rats.
- Fig. S6. BMI treatment reduces the neural response to noxious stimuli.
- Fig. S7. Schematic of acute thermal pain assays.
- Fig. S8. CPP results of CFA-treated YFP (control) rats.
- Fig. S9. Electrical deep brain stimulation (DBS) parameters.
- Fig. S10. BMI-driven DBS provides specific treatment for CFA rats without obvious side effects.
- Table S1. Comparison of the area under curve (AUC) among various non-noxious and noxious
- acute mechanical stimulus based on different LFP decoding strategies
- Table S2. Comparison of the AUC among various non-noxious and noxious stimulus using a CCF
- 442 decoding strategy

444 Other Supplementary Material for this manuscript includes the following:

445 Data file S1

446

447

443

REFERENCES AND NOTES

- 449 1. R. A. Andersen, T. Aflalo, S. Kellis, From thought to action: The brain-machine 450 interface in posterior parietal cortex. *Proceedings of the National Academy of Sciences* 451 **116**, 26274-26279 (2019).
- L. Grosenick, J. H. Marshel, K. Deisseroth, Closed-loop and activity-guided optogenetic control. *Neuron* **86**, 106-139 (2015).
- 454 3. M. M. Shanechi, Brain—machine interfaces from motor to mood. *Nature neuroscience* **22**, 455 1554-1564 (2019).
- G. K. Bergey, M. J. Morrell, E. M. Mizrahi, A. Goldman, D. King-Stephens, D. Nair, S.
 Srinivasan, B. Jobst, R. E. Gross, D. C. Shields, G. Barkley, V. Salanova, P. Olejniczak,
 A. Cole, S. S. Cash, K. Noe, R. Wharen, G. Worrell, A. M. Murro, J. Edwards, M.
- Duchowny, D. Spencer, M. Smith, E. Geller, R. Gwinn, C. Skidmore, S. Eisenschenk, M.
- Berg, C. Heck, P. Van Ness, N. Fountain, P. Rutecki, A. Massey, C. O'Donovan, D.
- Labar, R. B. Duckrow, L. J. Hirsch, T. Courtney, F. T. Sun, C. G. Seale, Long-term

- treatment with responsive brain stimulation in adults with refractory partial seizures. *Neurology* **84**, 810-817 (2015).
- 5. D. M. Taylor, S. I. Tillery, A. B. Schwartz, Direct cortical control of 3D neuroprosthetic devices. *Science* **296**, 1829-1832 (2002).
- 466 6. L. R. Hochberg, M. D. Serruya, G. M. Friehs, J. A. Mukand, M. Saleh, A. H. Caplan, A.
 467 Branner, D. Chen, R. D. Penn, J. P. Donoghue, Neuronal ensemble control of prosthetic
 468 devices by a human with tetraplegia. *Nature* 442, 164-171 (2006).
- F. B. Wagner, J. B. Mignardot, C. G. Le Goff-Mignardot, R. Demesmaeker, S. Komi, M.
 Capogrosso, A. Rowald, I. Seanez, M. Caban, E. Pirondini, M. Vat, L. A. McCracken, R.
 Heimgartner, I. Fodor, A. Watrin, P. Seguin, E. Paoles, K. Van Den Keybus, G. Eberle,
- 472 B. Schurch, E. Pralong, F. Becce, J. Prior, N. Buse, R. Buschman, E. Neufeld, N. Kuster, 473 S. Carda, J. von Zitzewitz, V. Delattre, T. Denison, H. Lambert, K. Minassian, J. Bloch,
- G. Courtine, Targeted neurotechnology restores walking in humans with spinal cord injury. *Nature* **563**, 65-71 (2018).
- F. R. Willett, D. T. Avansino, L. R. Hochberg, J. M. Henderson, K. V. Shenoy, Highperformance brain-to-text communication via handwriting. *Nature* **593**, 249-254 (2021).
- 478 9. A. I. Basbaum, D. M. Bautista, G. Scherrer, D. Julius, Cellular and molecular mechanisms of pain. *Cell* **139**, 267-284 (2009).
- 480 10. K. D. Davis, N. Aghaeepour, A. H. Ahn, M. S. Angst, D. Borsook, A. Brenton, M. E.
 481 Burczynski, C. Crean, R. Edwards, B. Gaudilliere, G. W. Hergenroeder, M. J. Iadarola, S.
 482 Iyengar, Y. Jiang, J. T. Kong, S. Mackey, C. Y. Saab, C. N. Sang, J. Scholz, M.
- Segerdahl, I. Tracey, C. Veasley, J. Wang, T. D. Wager, A. D. Wasan, M. A.
- Pelleymounter, Discovery and validation of biomarkers to aid the development of safe and effective pain therapeutics: challenges and opportunities. *Nat Rev Neurol* **16**, 381-486 400 (2020).
- 487 11. G. K. Anumanchipalli, J. Chartier, E. F. Chang, Speech synthesis from neural decoding of spoken sentences. *Nature* **568**, 493-498 (2019).
- 489 12. P. Rainville, G. H. Duncan, D. D. Price, B. Carrier, M. C. Bushnell, Pain affect encoded in human anterior cingulate but not somatosensory cortex. *Science* **277**, 968-971 (1997).
- J. P. Johansen, H. L. Fields, B. H. Manning, The affective component of pain in rodents:
 direct evidence for a contribution of the anterior cingulate cortex. *Proc Natl Acad Sci U S* A 98, 8077-8082 (2001).
- 494 14. S. C. LaGraize, J. Borzan, Y. B. Peng, P. N. Fuchs, Selective regulation of pain affect following activation of the opioid anterior cingulate cortex system. *Exp Neurol* **197**, 22-496 30 (2006).
- 497 15. R. a. C. Melzack, K.L., Sensory, motivational, and central control determinants of pain: a new conceptual model. . *The Skin Senses.*, 423-443 (1968).
- 499 16. R. Melzack, P. D. Wall, Pain mechanisms: a new theory. *Science* **150**, 971-979 (1965).
- 500 17. E. Navratilova, J. Y. Xie, A. Okun, C. Qu, N. Eyde, S. Ci, M. H. Ossipov, T. King, H. L. Fields, F. Porreca, Pain relief produces negative reinforcement through activation of
- 502 mesolimbic reward-valuation circuitry. *Proceedings of the National Academy of Sciences*503 of the United States of America **109**, 20709-20713 (2012).
- J. P. Johansen, H. L. Fields, Glutamatergic activation of anterior cingulate cortex produces an aversive teaching signal. *Nat Neurosci* **7**, 398-403 (2004).

- 506 19. Q. Zhang, T. Manders, A. P. Tong, R. Yang, A. Garg, E. Martinez, H. Zhou, J. Dale, A. Goyal, L. Urien, G. Yang, Z. Chen, J. Wang, Chronic pain induces generalized enhancement of aversion. *Elife* **6**, (2017).
- 509 20. H. Zhou, Q. Zhang, E. Martinez, J. Dale, S. Hu, E. Zhang, K. Liu, D. Huang, G. Yang, Z.
 510 Chen, J. Wang, Ketamine reduces aversion in rodent pain models by suppressing
 511 hyperactivity of the anterior cingulate cortex. *Nat Commun* 9, 3751 (2018).
- 512 21. G. Buzsáki, C. A. Anastassiou, C. Koch, The origin of extracellular fields and currents— 513 EEG, ECoG, LFP and spikes. *Nature reviews neuroscience* **13**, 407-420 (2012).
- 514 22. B. Pesaran, M. Vinck, G. T. Einevoll, A. Sirota, P. Fries, M. Siegel, W. Truccolo, C. E. Schroeder, R. Srinivasan, Investigating large-scale brain dynamics using field potential recordings: analysis and interpretation. *Nature neuroscience* **21**, 903-919 (2018).
- 517 23. L. Cao, V. Varga, Z. S. Chen, Spatiotemporal patterns of rodent hippocampal field potentials uncover spatial representations. *bioRxiv*, 828467 (2020).
- 519 24. A. Khorasani, N. H. Beni, V. Shalchyan, M. R. Daliri, Continuous force decoding from local field potentials of the primary motor cortex in freely moving rats. *Scientific reports* 521 **6**, 1-10 (2016).
- 522 25. S. D. Stavisky, J. C. Kao, P. Nuyujukian, S. I. Ryu, K. V. Shenoy, A high performing 523 brain—machine interface driven by low-frequency local field potentials alone and together 524 with spikes. *Journal of neural engineering* **12**, 036009 (2015).
- 525 26. C. D. Salzman, S. Fusi, Emotion, cognition, and mental state representation in amygdala and prefrontal cortex. *Annu Rev Neurosci* **33**, 173-202 (2010).
- 527 27. M. Moayedi, I. Weissman-Fogel, A. P. Crawley, M. B. Goldberg, B. V. Freeman, H. C. Tenenbaum, K. D. Davis, Contribution of chronic pain and neuroticism to abnormal forebrain gray matter in patients with temporomandibular disorder. *Neuroimage* 55, 277-530 286 (2011).
- 531 28. P. Y. Geha, M. N. Baliki, R. N. Harden, W. R. Bauer, T. B. Parrish, A. V. Apkarian, The 532 brain in chronic CRPS pain: abnormal gray-white matter interactions in emotional and 533 autonomic regions. *Neuron* **60**, 570-581 (2008).
- C. J. Kelly, M. Huang, H. Meltzer, M. Martina, Reduced Glutamatergic Currents and
 Dendritic Branching of Layer 5 Pyramidal Cells Contribute to Medial Prefrontal Cortex
 Deactivation in a Rat Model of Neuropathic Pain. Front Cell Neurosci 10, 133 (2016).
- 537 30. D. Radzicki, S. L. Pollema-Mays, A. Sanz-Clemente, M. Martina, Loss of M1 Receptor Dependent Cholinergic Excitation Contributes to mPFC Deactivation in Neuropathic Pain. *J Neurosci* **37**, 2292-2304 (2017).
- 540 31. G. Ji, V. Neugebauer, Pain-related deactivation of medial prefrontal cortical neurons involves mGluR1 and GABA(A) receptors. *J Neurophysiol* **106**, 2642-2652 (2011).
- 32. Z. Zhang, V. M. Gadotti, L. Chen, I. A. Souza, P. L. Stemkowski, G. W. Zamponi, Role
 of Prelimbic GABAergic Circuits in Sensory and Emotional Aspects of Neuropathic
 Pain. Cell Rep 12, 752-759 (2015).
- 545 33. M. Lee, T. R. Manders, S. E. Eberle, C. Su, J. D'Amour, R. Yang, H. Y. Lin, K. Deisseroth, R. C. Froemke, J. Wang, Activation of corticostriatal circuitry relieves chronic neuropathic pain. *J Neurosci* **35**, 5247-5259 (2015).
- 548 34. E. Martinez, H. H. Lin, H. Zhou, J. Dale, K. Liu, J. Wang, Corticostriatal Regulation of Acute Pain. *Front Cell Neurosci* **11**, 146 (2017).
- 550 35. S. G. Hardy, Analgesia elicited by prefrontal stimulation. *Brain Res* **339**, 281-284 (1985).

- 551 36. T. Kiritoshi, G. Ji, V. Neugebauer, Rescue of Impaired mGluR5-Driven Endocannabinoid 552 Signaling Restores Prefrontal Cortical Output to Inhibit Pain in Arthritic Rats. *J Neurosci* 553 **36**, 837-850 (2016).
- J. Dale, H. Zhou, Q. Zhang, E. Martinez, S. Hu, K. Liu, L. Urien, Z. Chen, J. Wang,
 Scaling Up Cortical Control Inhibits Pain. *Cell Rep* 23, 1301-1313 (2018).
- Z. Chen, Q. Zhang, A. P. Tong, T. R. Manders, J. Wang, Deciphering neuronal population codes for acute thermal pain. *J Neural Eng* **14**, 036023 (2017).
- Z. Q. Hu S, Wang J, Chen Z., A real-time rodent neural interface for deciphering acute
 pain signals from neuronal ensemble spike activity. *Proc. Asilomar Conf. Signals*,
 Systems & Computers, 93-97 (2017).
- A. Singh, D. Patel, A. Li, L. Hu, Q. Zhang, Y. Liu, X. Guo, E. Robinson, E. Martinez, L.
 Doan, B. Rudy, Z. S. Chen, J. Wang, Mapping Cortical Integration of Sensory and
 Affective Pain Pathways. *Curr Biol* 30, 1703-1715 e1705 (2020).
- L. L. Tan, M. J. Oswald, C. Heinl, O. A. Retana Romero, S. K. Kaushalya, H. Monyer, R.
 Kuner, Gamma oscillations in somatosensory cortex recruit prefrontal and descending
 serotonergic pathways in aversion and nociception. *Nat Commun* 10, 983 (2019).
- Z. Xiao, E. Martinez, P. M. Kulkarni, Q. Zhang, Q. Hou, D. Rosenberg, R. Talay, L.
 Shalot, H. Zhou, J. Wang, Z. S. Chen, Cortical Pain Processing in the Rat Anterior
 Cingulate Cortex and Primary Somatosensory Cortex. Front Cell Neurosci 13, 165
 (2019).
- Q. Zhang, Z. Xiao, C. Huang, S. Hu, P. Kulkarni, E. Martinez, A. P. Tong, A. Garg, H.
 Zhou, Z. Chen, J. Wang, Local field potential decoding of the onset and intensity of acute pain in rats. *Sci Rep* 8, 8299 (2018).
- 574 44. T. King, L. Vera-Portocarrero, T. Gutierrez, T. W. Vanderah, G. Dussor, J. Lai, H. L. Fields, F. Porreca, Unmasking the tonic-aversive state in neuropathic pain. *Nat Neurosci* **12**, 1364-1366 (2009).
- 577 45. E. Navratilova, J. Y. Xie, D. Meske, C. Qu, K. Morimura, A. Okun, N. Arakawa, M. Ossipov, H. L. Fields, F. Porreca, Endogenous opioid activity in the anterior cingulate cortex is required for relief of pain. *J Neurosci* **35**, 7264-7271 (2015).
- 580 46. S. G. Boccard, E. A. Pereira, L. Moir, T. Z. Aziz, A. L. Green, Long-term outcomes of deep brain stimulation for neuropathic pain. *Neurosurgery* **72**, 221-230; discussion 231 (2013).
- J. Spooner, H. Yu, C. Kao, K. Sillay, P. Konrad, Neuromodulation of the cingulum for neuropathic pain after spinal cord injury. Case report. *J Neurosurg* **107**, 169-172 (2007).
- 585 48. W. Lewin, C. W. Whitty, Effects of anterior cingulate stimulation in conscious human subjects. *J Neurophysiol* **23**, 445-447 (1960).
- 587 49. D. E. Richardson, H. Akil, Pain reduction by electrical brain stimulation in man. Part 1:
 588 Acute administration in periaqueductal and periventricular sites. *Journal of Neurosurgery*589 **47**, 178-183 (1977).
- 590 50. Y. Hosobuchi, J. E. Adams, R. Linchitz, Pain relief by electrical stimulation of the central gray matter in humans and its reversal by naloxone. *Science* **197**, 183-186 (1977).
- 592 51. I. M. Turnbull, R. Shulman, W. B. Woodhurst, Thalamic stimulation for neuropathic pain. *J Neurosurg* **52**, 486-493 (1980).
- 594 52. I. Decosterd, C. J. Woolf, Spared nerve injury: an animal model of persistent peripheral neuropathic pain. *Pain* **87**, 149-158 (2000).

- 53. S. Hu, Q. Zhang, J. Wang, Z. Chen, Real-time particle filtering and smoothing algorithms for detecting abrupt changes in neural ensemble spike activity. *J Neurophysiol* **119**, 1394-1410 (2018).
- C. Buchel, K. Bornhovd, M. Quante, V. Glauche, B. Bromm, C. Weiller, Dissociable neural responses related to pain intensity, stimulus intensity, and stimulus awareness within the anterior cingulate cortex: a parametric single-trial laser functional magnetic resonance imaging study. *The Journal of neuroscience : the official journal of the Society for Neuroscience* 22, 970-976 (2002).
- 604 55. W. D. Hutchison, K. D. Davis, A. M. Lozano, R. R. Tasker, J. O. Dostrovsky, Pain-605 related neurons in the human cingulate cortex. *Nat Neurosci* **2**, 403-405 (1999).
- 606 56. R. W. Sikes, B. A. Vogt, Nociceptive neurons in area 24 of rabbit cingulate cortex. *J Neurophysiol* **68**, 1720-1732 (1992).
- 57. S. J. Kang, C. Kwak, J. Lee, S. E. Sim, J. Shim, T. Choi, G. L. Collingridge, M. Zhuo, B.
 K. Kaang, Bidirectional modulation of hyperalgesia via the specific control of excitatory and inhibitory neuronal activity in the ACC. *Mol Brain* 8, 81 (2015).
- 611 58. Q. Zhang, S. Hu, R. Talay, Z. Xiao, D. Rosenberg, Y. Liu, G. Sun, A. Li, B. Caravan, A. Singh, J. D. Gould, Z. S. Chen, J. Wang, A prototype closed-loop brain-machine interface for the study and treatment of pain. *Nat Biomed Eng*, (2021).
- 614 59. R. D. Flint, Z. A. Wright, M. R. Scheid, M. W. Slutzky, Long term, stable brain machine 615 interface performance using local field potentials and multiunit spikes. *J Neural Eng* **10**, 616 056005 (2013).
- 61. S. R. Nason, A. K. Vaskov, M. S. Willsey, E. J. Welle, H. An, P. P. Vu, A. J. Bullard, C.
 61. S. Nu, J. C. Kao, K. V. Shenoy, T. Jang, H. S. Kim, D. Blaauw, P. G. Patil, C. A.
 61. Chestek, A low-power band of neuronal spiking activity dominated by local single units improves the performance of brain-machine interfaces. *Nat Biomed Eng* 4, 973-983 (2020).
- 622 61. R. P. Vertes, Interactions among the medial prefrontal cortex, hippocampus and midline thalamus in emotional and cognitive processing in the rat. *Neuroscience* **142**, 1-20 (2006).
- 625 62. A. E. Metz, H. J. Yau, M. V. Centeno, A. V. Apkarian, M. Martina, Morphological and functional reorganization of rat medial prefrontal cortex in neuropathic pain. *Proc Natl Acad Sci U S A* **106**, 2423-2428 (2009).
- J. Cheriyan, P. L. Sheets, Altered Excitability and Local Connectivity of mPFC-PAG
 Neurons in a Mouse Model of Neuropathic Pain. *J Neurosci* 38, 4829-4839 (2018).
- J. Huang, V. M. Gadotti, L. Chen, I. A. Souza, S. Huang, D. Wang, C. Ramakrishnan, K.
 Deisseroth, Z. Zhang, G. W. Zamponi, A neuronal circuit for activating descending
 modulation of neuropathic pain. *Nat Neurosci* 22, 1659-1668 (2019).
- 633 65. R. M. Levy, S. Lamb, J. E. Adams, Treatment of chronic pain by deep brain stimulation: long term follow-up and review of the literature. *Neurosurgery* **21**, 885-893 (1987).
- 635 66. Z. Xiao, S. Hu, Q. Zhang, X. Tian, Y. Chen, J. Wang, Z. Chen, Ensembles of change-636 point detectors: implications for real-time BMI applications. *J Comput Neurosci* **46**, 107-637 124 (2019).
- 638 67. D. J. Langford, A. L. Bailey, M. L. Chanda, S. E. Clarke, T. E. Drummond, S. Echols, S.
 639 Glick, J. Ingrao, T. Klassen-Ross, M. L. Lacroix-Fralish, L. Matsumiya, R. E. Sorge, S.
 640 G. Sotocinal, J. M. Tabaka, D. Wong, A. M. van den Maagdenberg, M. D. Ferrari, K. D.

- 641 Craig, J. S. Mogil, Coding of facial expressions of pain in the laboratory mouse. *Nat Methods* 7, 447-449 (2010).
- 643 68. S. Alomar, N. K. King, J. Tam, A. A. Bari, C. Hamani, A. M. Lozano, Speech and language adverse effects after thalamotomy and deep brain stimulation in patients with movement disorders: A meta-analysis. *Mov Disord* 32, 53-63 (2017).
- 646
 69. A. Beric, P. J. Kelly, A. Rezai, D. Sterio, A. Mogilner, M. Zonenshayn, B. Kopell,
 647 Complications of deep brain stimulation surgery. *Stereotactic and functional* 648 *neurosurgery* 77, 73-78 (2001).
- H. Bokil, P. Andrews, J. E. Kulkarni, S. Mehta, P. P. Mitra, Chronux: a platform for analyzing neural signals. *Journal of neuroscience methods* **192**, 146-151 (2010).

653654

651 71. G. Sun, Z. Wen, D. Ok, L. Doan, J. Wang, Z. S. Chen, Detecting acute pain signals from human EEG. *J Neurosci Methods* **347**, 108964 (2021).

FIGURE LEGENDS

655

656

657

658

659

660

661

662

663

664

665

666

667

668

669

670

671

672

673

674

675

676

Fig. 1. Design of a multi-region LFP-based neural interface for pain.

(A) Schematic of experiments. The online closed-loop brain-machine interface (BMI) consists of three steps. In step (1), silicon probe arrays are implanted in the rat anterior cingulate cortex (ACC) and primary somatosensory cortex (S1) to record local field potentials (LFPs) simultaneously. In step (2), LFP signals are processed and sent to an automated decoder based on a state space model (SSM) to detect the onset of pain. In step (3), detected pain onset triggers neurofeedback in the form of optogenetic or electrical activation of the prelimbic prefrontal cortex (PL-PFC) to deliver pain modulation. (B) Placement of optic fiber or deep brain stimulating (DBS) electrode in the PL-PFC and recording silicon probes in the ACC and S1. (C) Raw LFP signals were processed to compute three band-limited LFP power features for the ACC channel: $\{y_{1,k}^{ACC}, y_{2,k}^{ACC}, y_{3,k}^{ACC}\}$ and S1 channel: $\{y_{1,k}^{S1}, y_{2,k}^{S1}, y_{3,k}^{S1}\}$, where the index k denotes the k-th temporal window (bin size 100 ms). MUA: multi-unit activity (300-500 Hz). (D) Schematic of two SSMs used to independently infer the latent variables $\{z_k^{ACC}\}v$ and $\{z_k^{S1}\}$ from the LFP features $\{Y_k^{ACC}\}$ and $\{Y_k^{S1}\}$ of ACC and S1, respectively (see Supplementary Materials and Methods for details). The SSM is illustrated by a graphical model with a Markovian structure, in which each node denotes a random variable, and the arrow indicates statistical dependency between two random variables. (E) Illustration of a multi-region decoding strategy for pain onset. First, the Z-scores were derived from the latent variables $\{z_k^{\text{ACC}}\}$ and $\{z_k^{\text{S1}}\}$ (horizontal dashed lines denote the 95% confidence intervals for statistical significance). Next, a moving average cross-correlation function (CCF) was used to compute the correlation between the two Z-score series. The area beyond statistical significance (horizontal dashed lines) was computed to determine the change point (Supplementary Materials

- and Methods). When pain onset was detected, the decoder automatically triggered optogenetic or
- DBS stimulation to activate the PL-PFC.

Fig. 2. The multi-region LFP-based neural interface inhibits acute mechanical and thermal pain.

679

680

681

682

683

684

685

686

687

688

689

690

691

692

693

694

695

696

697

698

699

700

701

(A) Schematic of pain experiments demonstrating peripheral stimulation with either pin prick (PP) or von Frey filament (vF). LFP signals were recorded from ACC and S1 for pain detection, and optogenetic stimulation was administered to the PL-PFC for pain control. (B) Withdrawal response to mechanical stimulation, n = 10 rats; ****P < 0.0001, Wilcoxon Signed Rank test. (C) Illustration of mechanical pain onset detection using an LFP-based strategy. LFP features were computed from the ACC, S1, or both ACC and S1. The top two panels show single-channel LFP traces (white) overlying the spectrogram. The vertical dotted line indicates the onset of noxious peripheral stimulus (PP), and the vertical solid line indicates the time of paw withdrawal. The third and fourth panels show Z-scores (shaded areas denote the 95% confidence intervals) derived from the SSM-based decoder using LFPs recorded from ACC and S1, respectively (Methods). The two horizontal lines indicate the Z-score threshold \pm 3.38. The fifth panel shows the cross-correlation function (CCF) between ACC and S1 from the third and fourth panels. The two horizontal dashed lines indicate the significance threshold. The bold triangle indicates the detection point. (D) Similar to panel c, except that the stimulus given is non-noxious (vF). (E) Demonstration of continuous online pain onset detection in a sample recording session. The vertical dotted line indicates the stimulus onset, and the vertical solid line indicates paw withdrawal. ♦ denotes true pain detection, * denotes false detection. (F) Comparison of detection rates between various non-noxious stimuli and noxious PP based on LFP decoding strategies using the ACC, S1 and combined (ACC + S1) signals. Each circle indicates data from one rat, n = 5 rats; ns, P > 0.05, **P < 0.01, ***P < 0.001and ****P < 0.0001, one-way ANOVA with repeated measures and post-hoc Tukey's multiple comparison tests to compare decoding rates for 2g vF, 6g vF, PP stimulation using signals from

the ACC, S1 or ACC+S1. (G) The false positive (FP) detection rate per minute. n = 5 rats; P = 0.9679 (ACC vs S1), **P = 0.0036 (ACC vs ACC+S1), **P = 0.0036 (S1 vs ACC+S1), one-way ANOVA with repeated measures and post-hoc Tukey's multiple comparison tests. (H) Comparison of detection rates based on LFP signals recorded in two different sessions, 3 months apart. Session 2 was recorded 3 months after session 1. Each pair of circles connected by a line indicates data from the same rat. We used the first 1-3 trials of each recording session to train the parameters of the SSM. n = 5 rats; *P = 0.0148 (ACC), P = 0.4651 (S1), P = 0.8650 (ACC+S1), paired t-test. (I) Comparison of detection rates based on model parameters set 5 days apart. We used the first 3 trials on Day 1 to train the parameters of SSM, and then used these same parameters to detect pain on the subsequent 5 days. n = 5 rats; P = 0.2339, one-way ANOVA with repeated measures and *post-hoc* Tukey's multiple comparison tests.

714 Fig. 3. The multi-region LFP-based neural interface inhibits acute mechanical pain

715 (A) Schematic of conditioned place preference (CPP) assays to assess pain aversion. In a two-716 chamber set up, during conditioning, one of the chambers was paired with treatment shown in red, 717 and the opposite chamber was paired with control conditions shown in brown (see Supplementary 718 Materials and Methods for details). (B) Left panel: Time spent in preconditioning and testing phases in BMI+PP vs random+PP paired chambers, n = 5 rats; **P = 0.0016, paired t-test. Right 719 720 panel: comparison of CPP scores of ChR2-expressing and YFP-expressing (control) rats (n = 5721 ChR2 rats and 5 YFP rats, **P = 0.0027, unpaired t-test). (C) Left panel: Time spent in 722 preconditioning and testing phases in manual+PP vs random+PP paired chambers, n = 5 rats; *P = 0.013, paired t-test. Right panel: comparison of CPP scores of ChR2 and YFP rats (n = 5 ChR2 723 724 rats and 5 YFP rats, **P = 0.0036, unpaired t-test). (D) Left panel: Time spent in preconditioning 725 and testing phases in BMI+PP vs manual+PP paired chambers, n = 5 rats; P = 0.74, paired t-test. 726 Right panel: comparison of CPP scores of ChR2 and YFP rats (n = 5 ChR2 rats and 5 YFP rats, P 727 = 0.969, unpaired t-test). (E) Left panel: Time spent in preconditioning and testing phases in 728 BMI+6g vF vs random+6g vF paired chambers, n = 5 rats; P = 0.46, paired t-test. Right panel: 729 comparison of CPP scores of ChR2 and YFP rats (n = 5 ChR2 rats and 5 YFP rats, P = 0.428,

730

unpaired t-test).

Fig. 4. The multi-region neural interface inhibits acute thermal pain

731

747

732 (A) Schematic of thermal stimulation experiments, with infrared intensity (IR) set to either 70 (noxious) or 10 (non-noxious). (B) IR 70 elicited paw withdrawals. n = 10 rats; ****P < 0.0001, 733 734 Wilcoxon Signed Rank test. (C, D) Illustration of thermal pain onset detection using an LFP-based 735 strategy, similar to panels 2C and 2D. (E) Comparison of the detection rate based on LFP decoding 736 strategies using the ACC, S1, and combined (ACC + S1) signals. Each circle indicates data from 737 a single rat. Comparison of the detection rates for three LFP-based decoding strategies. n = 5 rats; ns, P > 0.05, ***P < 0.001, ****P < 0.0001, one-way ANOVA with repeated measures and post-738 739 hoc Tukey's multiple comparison tests to compare decoding rates for IR 10, 20, 70 using signals 740 from ACC, S1 or ACC+S1. (F) Comparison of paw withdrawal latency for ChR2 rats. n = 5 rats; **P = 0.0089 (No opto vs BMI opto), **P = 0.0044 (No opto vs Manual opto), P = 0.9176 (BMI 741 742 opto vs Manual opto), one-way ANOVA with repeated measures and post-hoc Tukey's multiple 743 comparison tests. (G) Comparison of paw withdrawal latency for YFP control rats. n = 5 rats; P =744 0.5385 (No opto vs BMI opto), P = 0.9741 (No opto vs Manual opto), P = 0.7909 (BMI opto vs 745 Manual opto), one-way ANOVA with repeated measures and post-hoc Tukey's multiple 746 comparison tests.

748 Fig. 5. The multi-region neural interface performance in a chronic inflammatory pain model 749 750 (A) Schematic of experiments in CFA-treated rats. (B) CFA injection caused mechanical allodynia, 751 n = 10 rats (5 ChR2 rats and 5 YFP rats); ****P < 0.0001, one-way ANOVA with repeated 752 measures and post-hoc Tukey's multiple comparison tests. (C) Paw withdrawal rate with vF stimulation. n = 10 rats, ****P < 0.0001, paired t-test. (**D**) Illustration of the multi-region LFP-753 754 based strategy for detecting the onset of evoked pain signal in a CFA-treated rat. Similar to panels 755 2C and 2D. (E) A comparison of different LFP-based strategies for decoding the pain onset in the 756 CFA model. Comparison of the detection rates for the noxious vs non-noxious stimulus, n = 10rats, ****P < 0.0001, paired t-test. Comparison of the detection rates for three LFP-based decoding 757 758 strategies. For the noxious stimulus: n = 10 rats; P = 0.8139 (ACC vs S1), P = 0.9993 (ACC vs 759 ACC+S1), P = 0.8231 (S1 vs ACC+S1). For the noxious stimulus: n = 10 rats; P = 0.4975 (ACC 760 vs S1), *P = 0.0250 (ACC vs ACC+S1), **P = 0.0023 (S1 vs ACC+S1), one-way ANOVA with 761 repeated measures and post-hoc Tukey's multiple comparison tests. (F) Multi-region LFP-based BMI inhibited mechanical allodynia in CFA-treated rats. n = 5 rats; **P = 0.0026, paired t-test. 762 763

Fig. 6. The multi-region neural interface inhibits chronic inflammatory pain

764

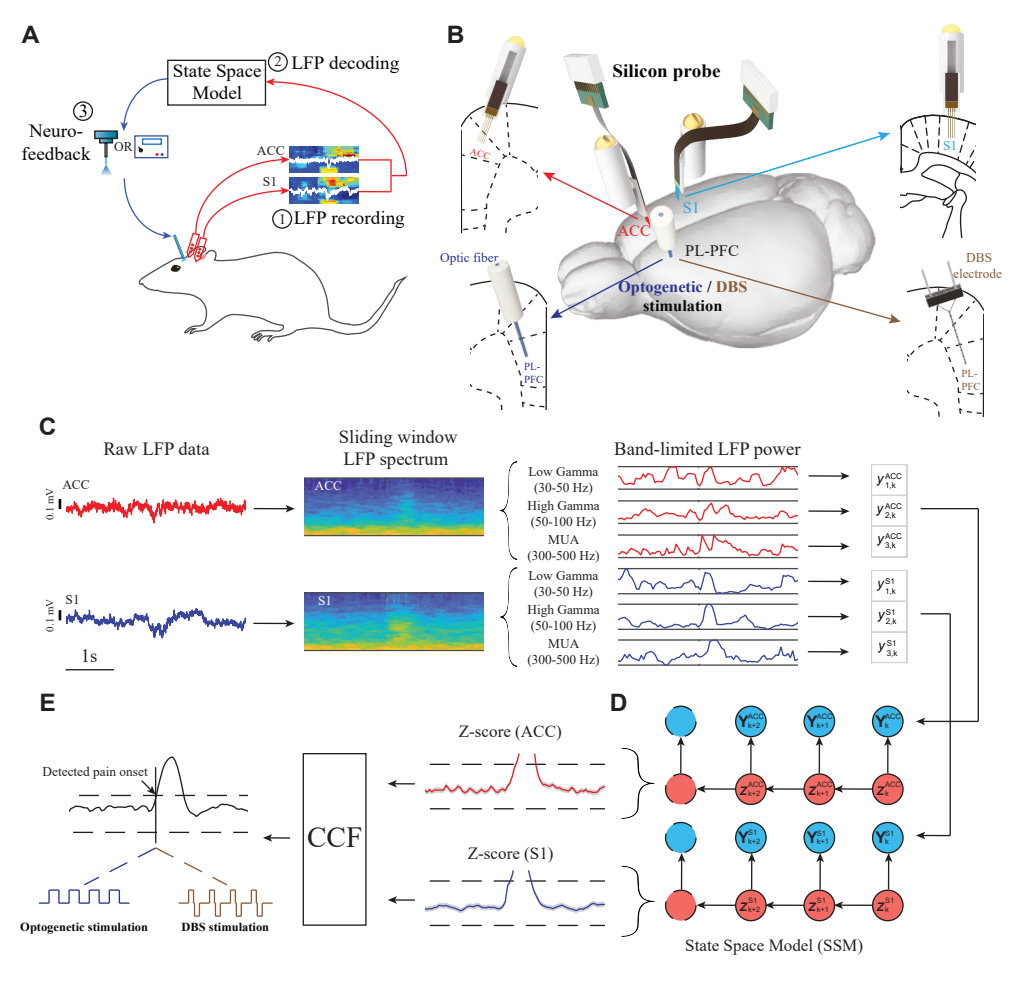
765 (A) Schematic of CPP assays in CFA-treated rats. 6g vF represents noxious stimulation, 0.4g vF 766 represents non-noxious stimulation. (B) Time spent in preconditioning and testing phases in 767 chambers paired with BMI+6g vF vs random+6g vF, n = 5 rats; *P = 0.028, paired t-test. (C) 768 Comparison of CPP scores of ChR2 and YFP rats, n = 5 rats; *P = 0.015, unpaired t-test. (**D**) Time 769 spent in preconditioning and testing phases in chambers paired with BMI+0.4g vF vs random+0.4g vF, n = 5 rats; P = 0.392, paired t-test. (E) Comparison of CPP scores of ChR2 and YFP rats, n = 10770 771 5 rats; P = 0.527, unpaired t-test. (F) Schematic of the CPP experiment to test tonic pain in CFA-772 treated rats. No peripheral stimuli were given. One chamber was paired with closed-loop BMI 773 treatment, and the opposite chamber was paired with random PL-PFC activation of matching 774 duration and intensity. (G) Demonstration of continuous decoding for spontaneous pain detection 775 in the absence of peripheral stimuli. The first and second panels show the Z-score (shaded area 776 denotes the 95% confidence intervals) derived from the LFP-based SSM decoder, where two 777 horizontal dotted lines indicate the Z-score threshold \pm 3.38. The third panel shows the cross-778 correlation function (CCF) between the two Z-scores. Two horizontal dashed lines indicate the 779 significance threshold. The two black triangles mark the detection onset of spontaneous pain. (H) 780 Time spent in preconditioning and testing phases in chambers paired with BMI vs random 781 stimulation, n = 5 rats; *P = 0.0266, paired t-test. (I) Comparison of CPP scores of ChR2 and YFP rats, n = 5 rats; **P = 0.0087, unpaired t-test. 782

783 Fig. 7. A BMI-driven, closed-loop DBS inhibits acute and chronic inflammatory pain.

(A) Placement of stimulating electrode in the PL-PFC and recording electrodes in the ACC and S1. (B) Schematic of pain experiments during mechanical stimulus delivery. (C) Schematic of CPP experiments to assess aversion to evoked pain using DBS. (D) Time spent in preconditioning and testing phase in chambers paired with BMI+PP vs random+PP, n = 7 rats; *P = 0.0207, paired t-test. (E) Schematic of thermal experiments in DBS rats. Top panel: schematic of the Hargreaves test (IR 70). Bottom panel: comparison of paw withdrawal latency during different experimental conditions. n = 7 rats; ****P = 0.001, paired t-test. (F) Top panel: schematic of the experiment. Bottom panel: 50% paw withdrawal threshold in the presence of BMI-driven DBS vs control (no DBS). n = 7 rats; ****P < 0.0001, paired t-test. (G) Schematic of the CPP assay to assess aversion to evoked pain. (H) Time spent in preconditioning and testing phases in chambers paired with BMI+vF vs random+vF, n = 7 rats; *P = 0.0194, paired t-test. (I) Schematic of the CPP experiment to test tonic pain in CFA-treated rats. (J) Time spent in preconditioning and testing phases in chambers paired with BMI vs random DBS, n = 7 rats; ****P < 0.0001, paired t-test.

798 Fig. 8. Closed-loop BMI reduces chronic neuropathic pain. 799 800 (A) Schematic of pain experiments in SNI-treated rats. (B) SNI operation resulted in mechanical allodynia, n = 5 rats; ****P < 0.0001, one-way ANOVA with repeated measures and post-hoc 801 Tukey's multiple comparison tests. (C) Multi-region LFP-based BMI inhibited mechanical 802 allodynia in SNI-treated rats. n = 5 rats; ***P = 0.0004, paired t-test. (**D**) Schematic of the CPP 803 804 experiment to test tonic pain in SNI-treated rats.. (E) Time spent in preconditioning and testing phases in chambers paired with BMI vs random DBS, n = 5 rats; *P = 0.0231, paired t-test. 805 806 807

Fig. 1



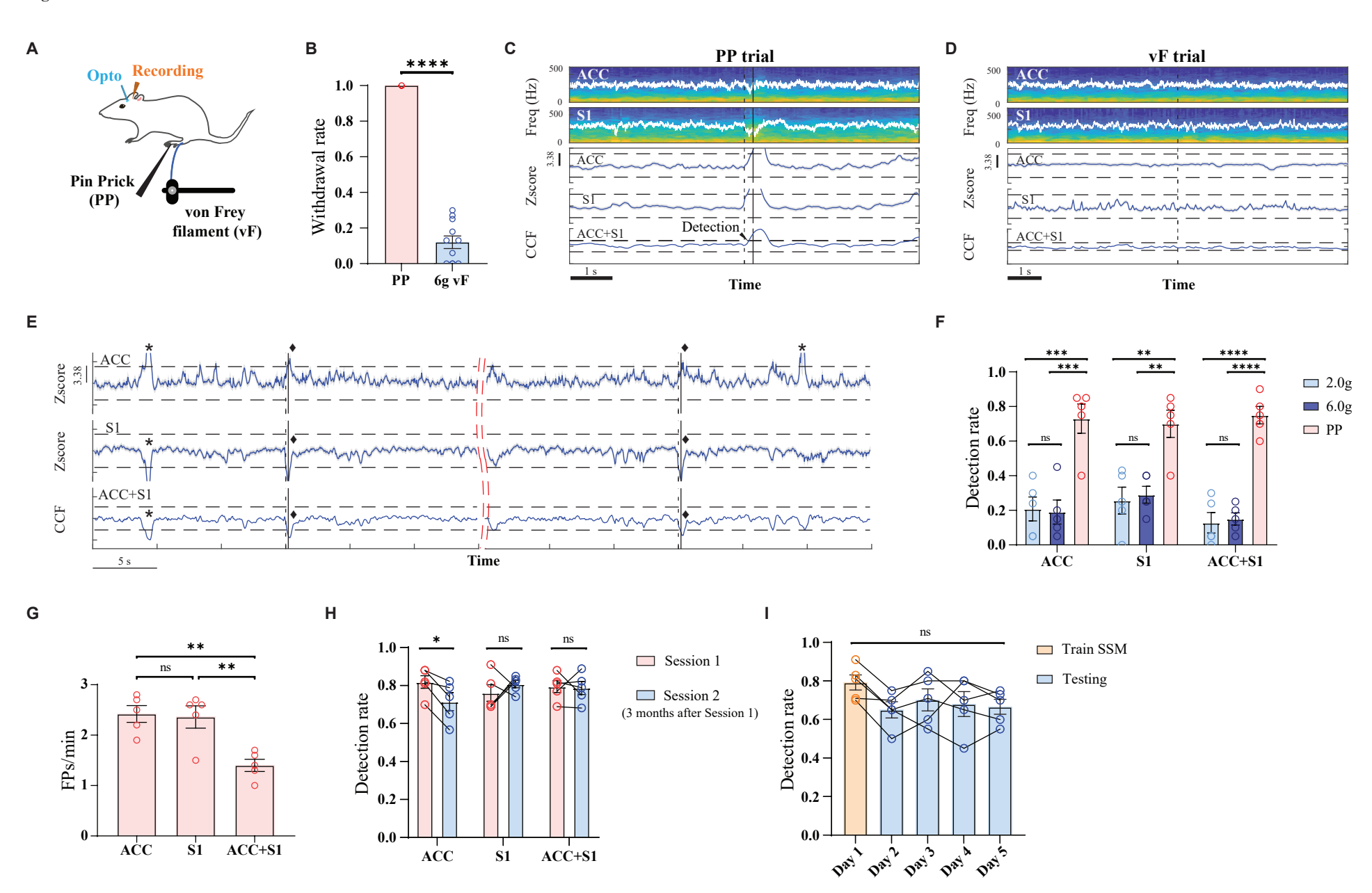


Fig. 3

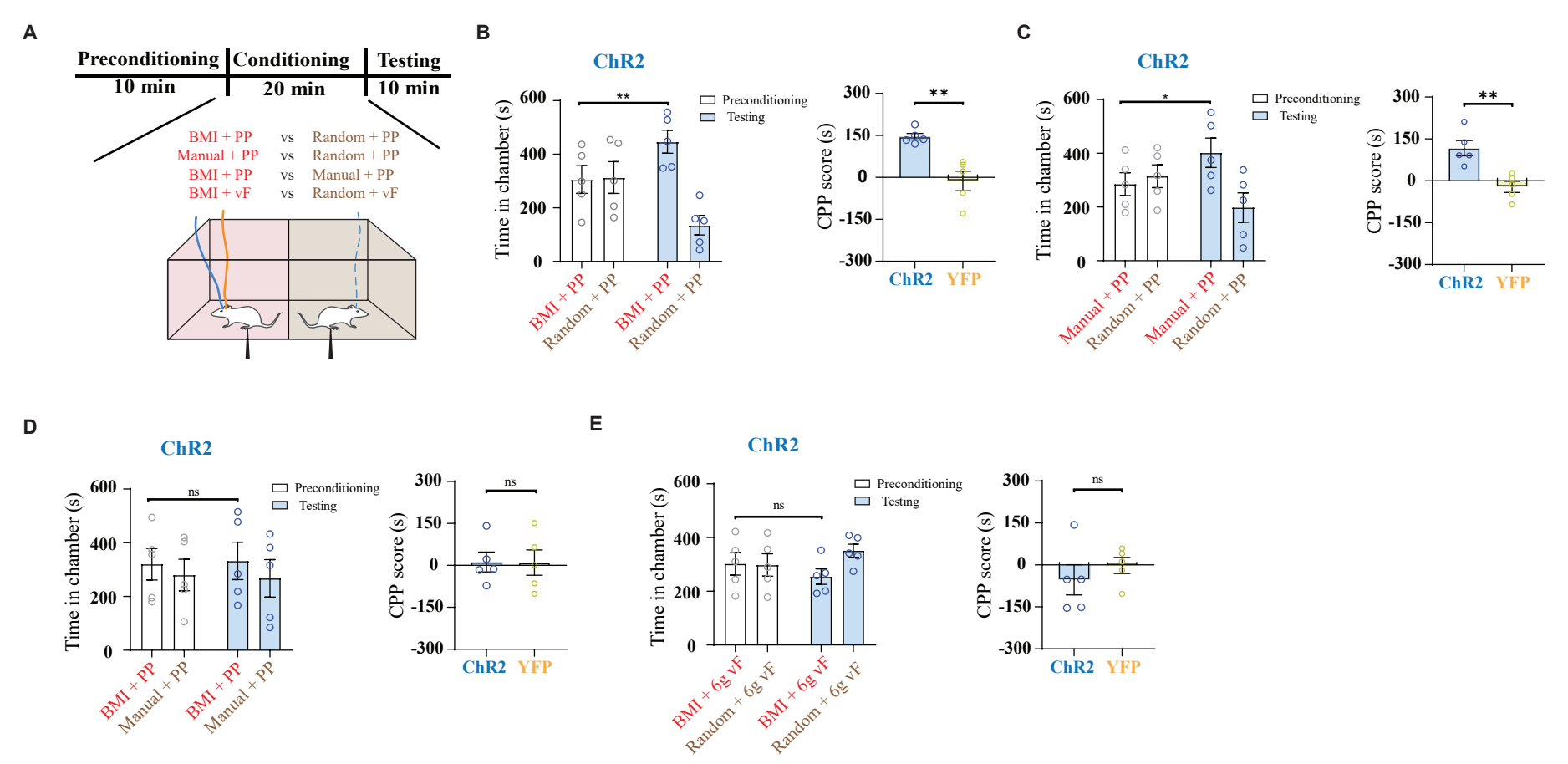


Fig. 4

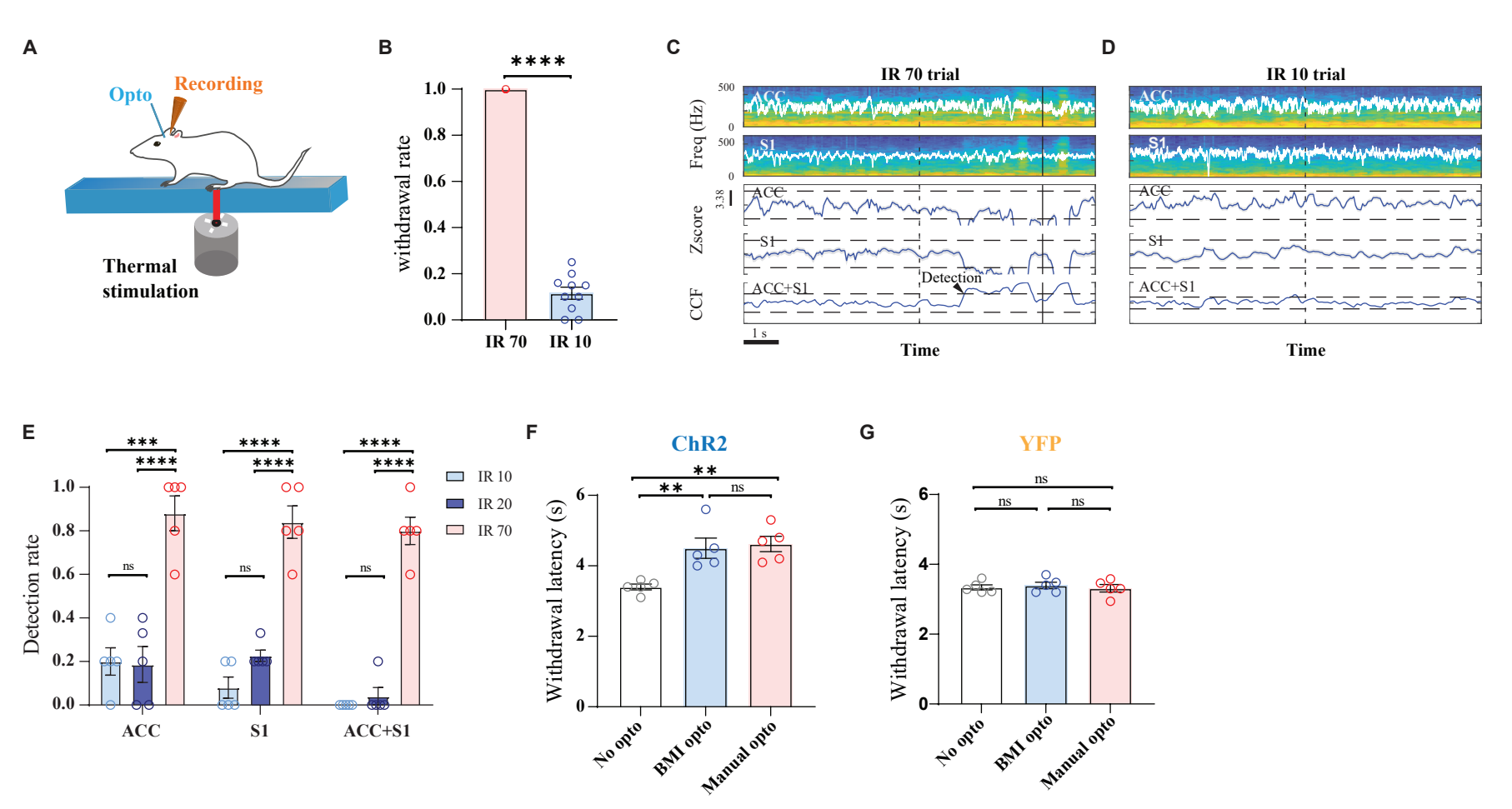


Fig. 5

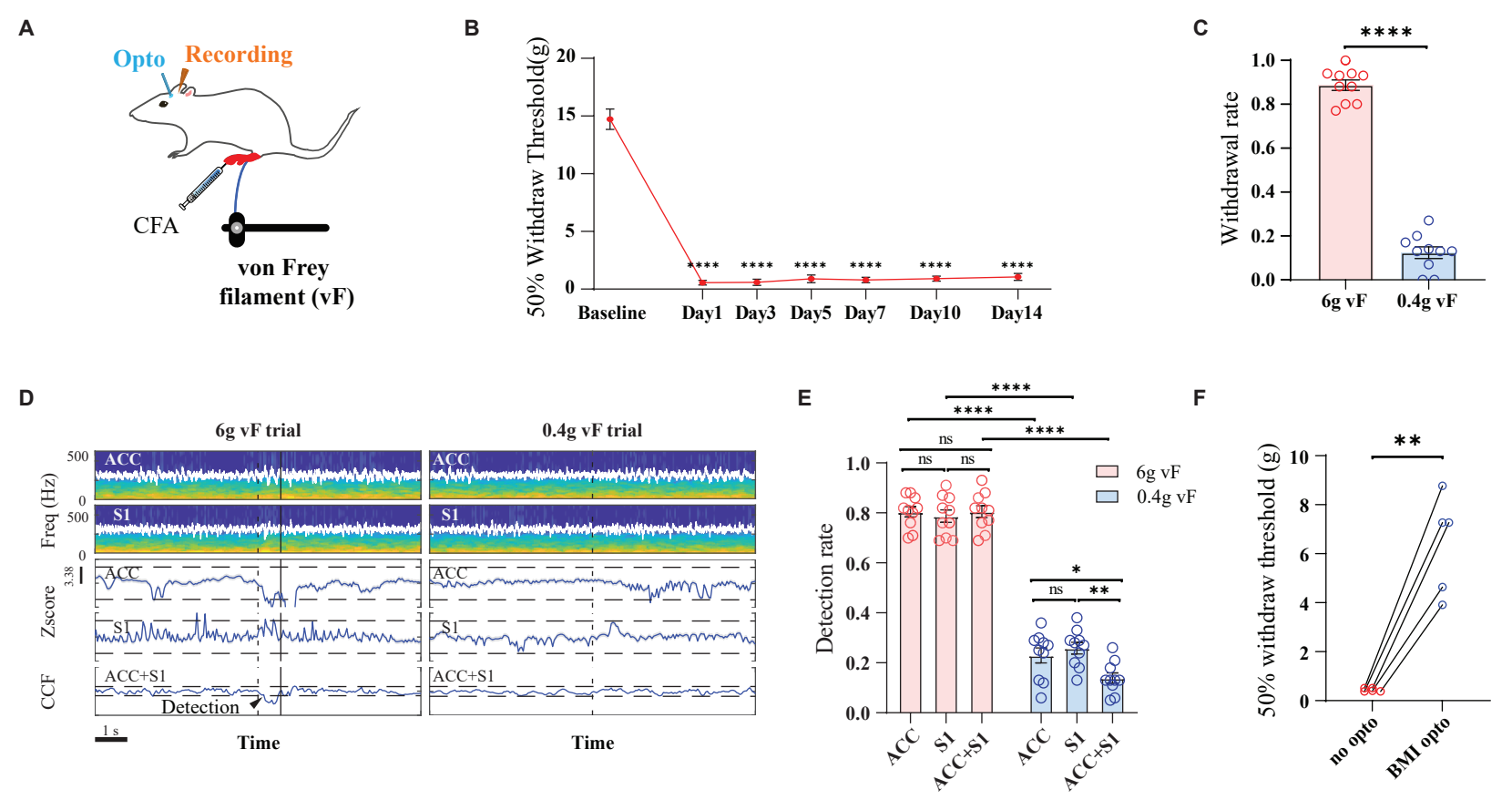
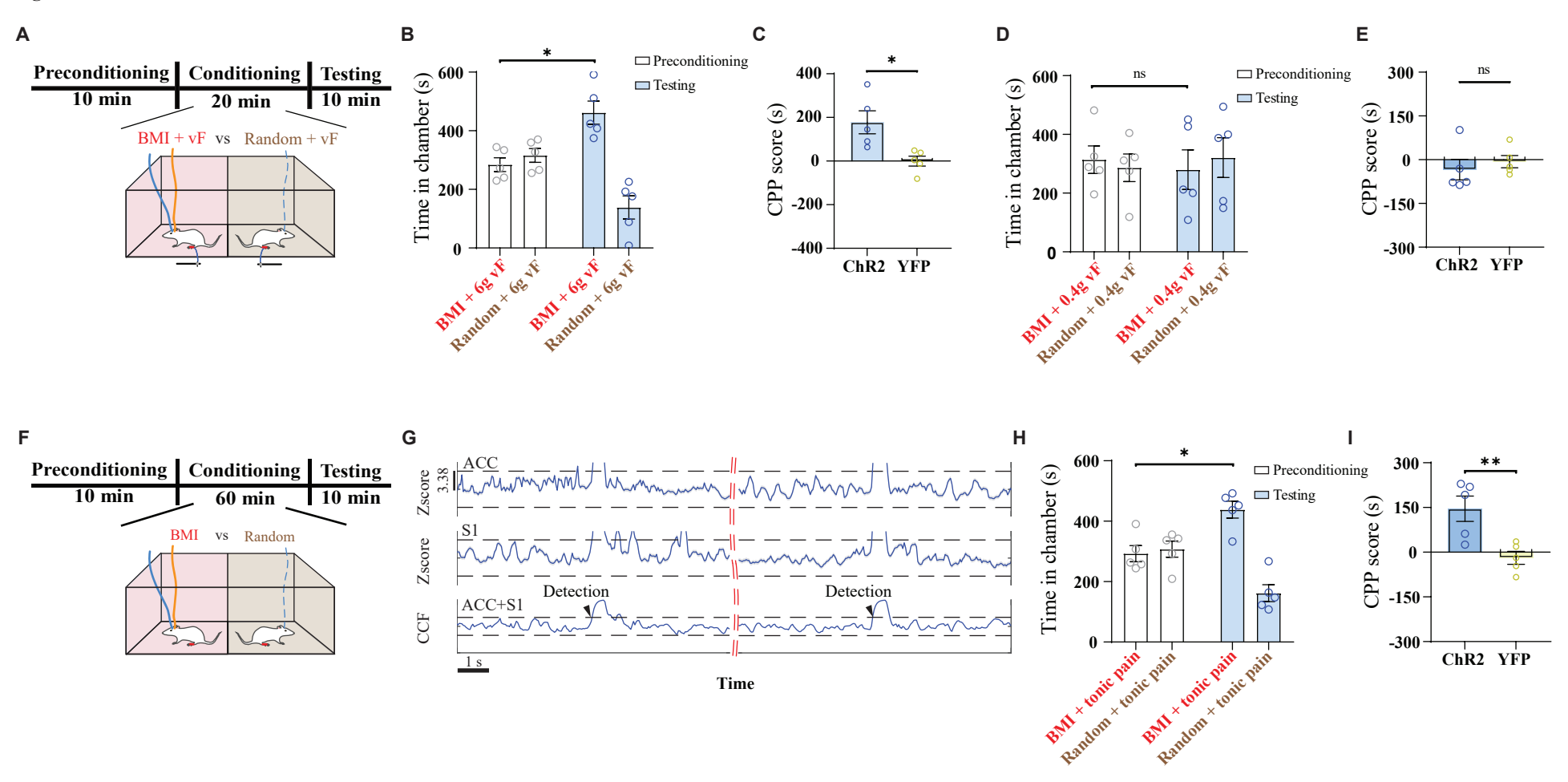


Fig. 6



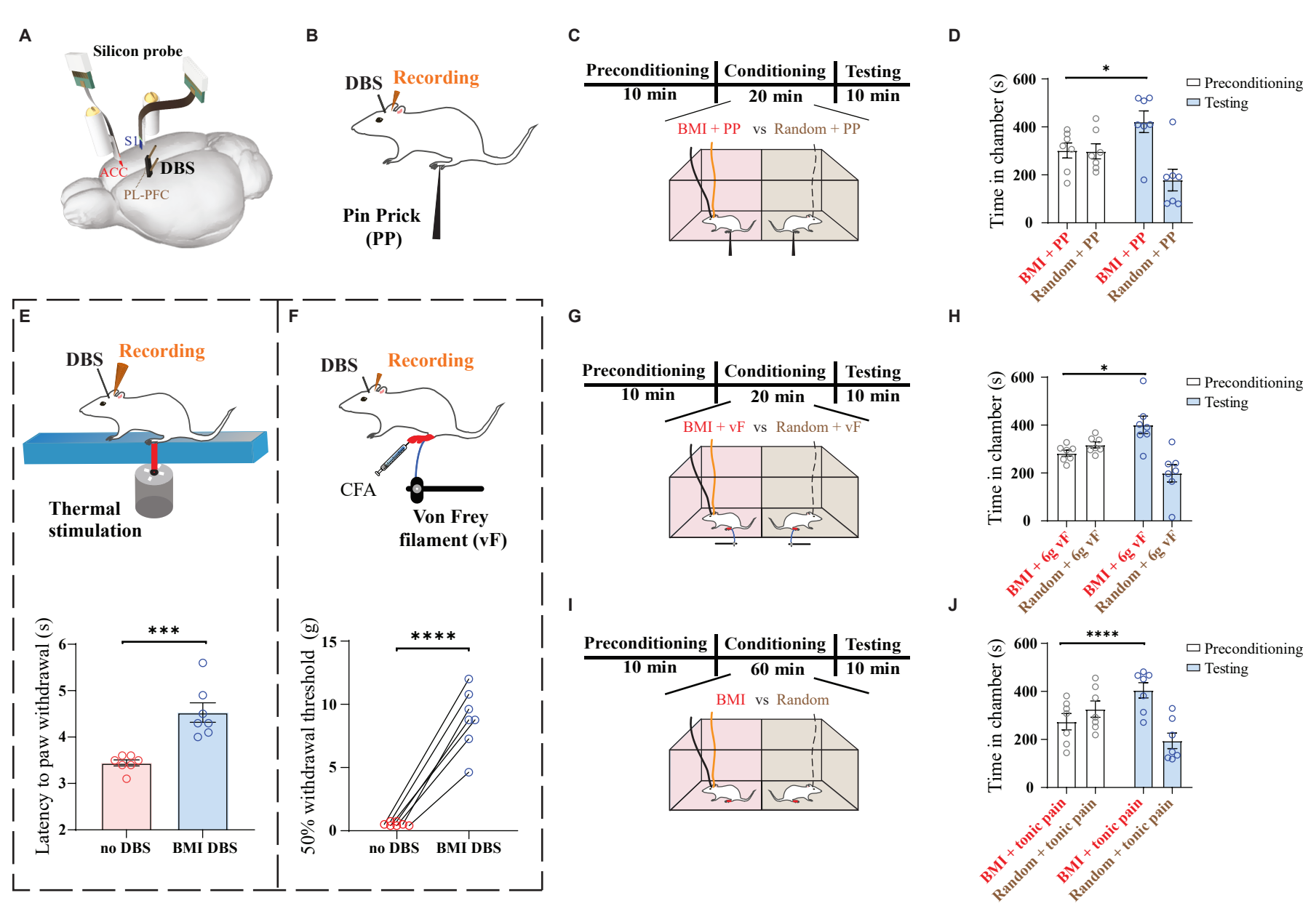
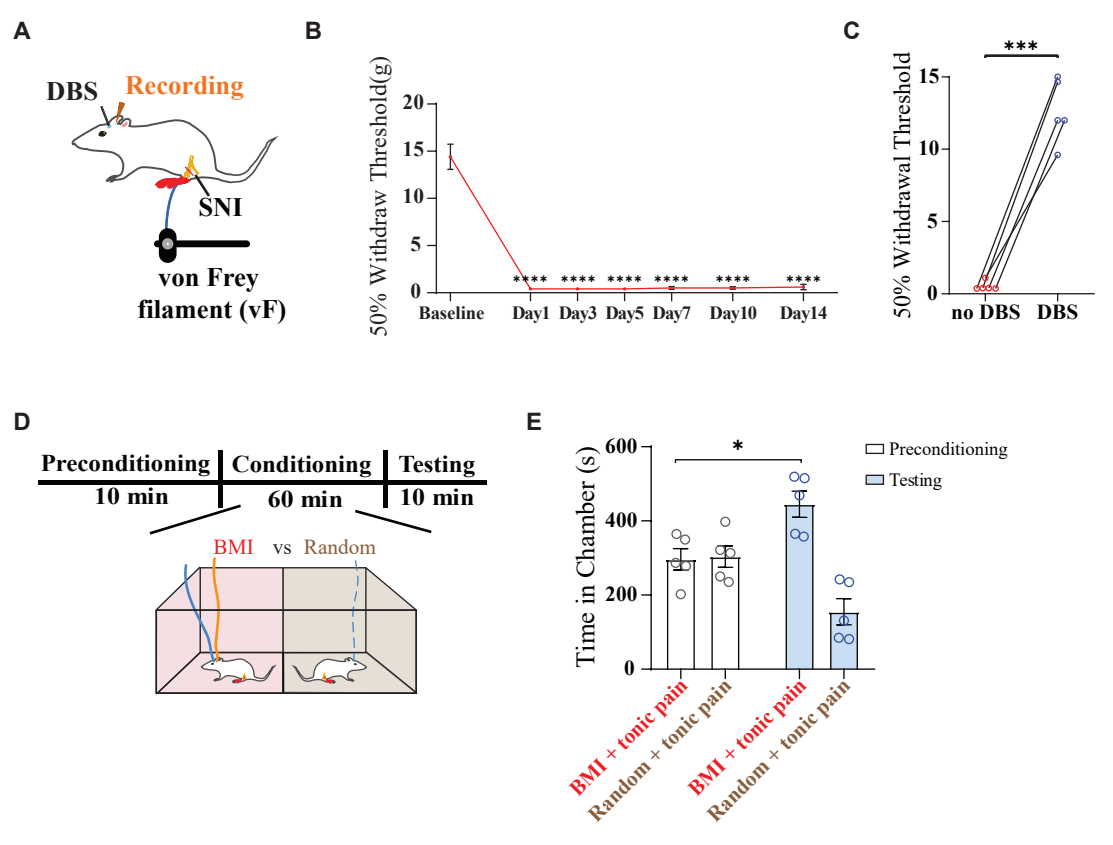


Fig. 8



1	Supplementary Materials for		
2	A multi-region neural interface for analgesic delivery		
3	Guanghao Sun ^{1,2,3} , Fei Zeng ² , Michael McCartin ² , Qiaosheng Zhang ^{2,3} , Helen Xu ² , Yaling Liu ² ,		
4	Zhe Sage Chen ^{1,3,4,5,*} , Jing Wang ^{2,3,4,5} *		
5			
6 7	The PDF file includes: Materials & Methods		
8	Fig. S1. Histology showing viral expression, and optic fiber and silicon probe implantations.		
9	Fig. S2. Schematic of software design for a closed-loop multi-region LFP-based BMI.		
10	Fig. S3. Pain-evoked event-related potentials (ERPs) analysis.		
11	Fig. S4. False detection rate in cross session analysis.		
12	Fig. S5. LFP-based BMI does not alter pain-aversive behaviors in YFP-treated (control) rats.		
13	Fig. S6. BMI treatment reduces the neural response to noxious stimuli.		
14	Fig. S7. Schematic of acute thermal pain assays.		
15	Fig. S8. CPP results of CFA-treated YFP (control) rats.		
16	Fig. S9. Electrical deep brain stimulation (DBS) parameters.		
17	Fig. S10. The BMI-driven DBS provides specific treatment for CFA rats without obvious side		
18	effects.		
19	Table S1. Comparison of the area under curve (AUC) between various non-noxious and noxious		
20	acute mechanical stimulus based on different LFP decoding strategies		
21	Table S2. Comparison of the AUC between various non-noxious and noxious stimulus using a		
22	CCF decoding strategy		
23			
24	Other Supplementary Material for this manuscript includes the following:		
25	Data file S1 (Microsoft Excel format). Raw data.		

MATERIALS & METHODS

- 28 Experimental protocol, data acquisition and BMI system architecture
- 29 All experimental studies were performed in accordance with the New York University School of
- 30 Medicine (NYUSOM) Institutional Animal Care and Use Committee (IACUC) to ensure minimal
- animal use and discomfort, license reference number: IA16-01388. Male Sprague-Dawley rats
- 32 were purchased from Taconic Farms and kept at the vivarium facility in the NYU Langone Science
- Building, with controlled humidity, temperature, and 12-hr (6:30 AM–6:30 PM) light-dark cycle.
- Food and water were available *ad libitum*. Animals weighed 250 to 300 g upon arrival to the
- 35 facility and were given 10 days on average to adjust to the new environment before the initiation
- of experiments.

37

38

27

Virus construction and packaging

- 39 Recombinant AAV (adeno-associated virus) vectors were serotyped with AAV1 coat proteins, and
- 40 packaged at Addgene viral vector manufacturing facilities. Viral titers were 5×10¹² particles/ml
- 41 for AAV1.CaMKII.ChR2-eYFP.WPRE.hGH, and AAV1.CaMKII(1.3).eYFP.WPRE.hGH.

42

43

Viral injection

- Before viral injection, rats were anesthetized with isoflurane (1.5 to 2%). In all experiments, the
- 45 virus, as specified above, was delivered selectively to the prelimbic PFC (PL-PFC). We used a 26-
- 46 gauge 1 µL Hamilton syringe to inject 0.7 µL of the viral vector into the rat's cortex at
- anteroposterior (AP) ± 2.9 mm, mediolateral (ML) ± 1.6 mm, and dorsoventral (DV) ± 3.7 mm, with
- 48 injector tips angled 17° toward the midline. The injection rate was kept at approximately 0.1 μl
- 49 per 10 seconds. Afterwards, we left the microinjection needle in place for 10 minutes, raised it by
- 50 1 mm, and left the needle in place for an additional 5 minutes. This minimized the spread of viral

particles along the injection tract and allowed for uniform diffusion of the virus at the injection site. After the viral injection, the scalp was sutured, and the rats were given 2-4 weeks for recovery before optic fiber and electrode implantation.

54

55

56

57

58

59

60

61

62

63

64

65

66

67

68

69

70

53

51

52

Prelimbic PFC optic fiber and silicon probe implantation surgery

Optic fiber and electrode implantation surgery has been described in previous studies (37, 40). We designed a customized fiber optic ferrule to hold a 200 µm fiber in a 2.5 mm ferrule (Thorlabs) for PL-PFC optogenetic stimulation. Two 32-channel silicon probes (Buzsaki32-H32, NeuroNexus Technologies, or ASSY-116 E-1, Cambridge NeuroTech) were glued to 3D printed custom design drives, one used for ACC recordings, and the other for S1 recordings. During the implantation surgery, rats were anesthetized with isoflurane (1.5 to 2%). The silicon probes were implanted in the ACC (AP +2.7 mm, ML±1.6 mm, DV -2.0 mm with tips angle 20° toward the midline, fig. S1A) and the S1 (AP -1.5 mm, ML ± 3.0 mm, DV -1.1 mm with angle 0°, fig. S1B). Optic fiber was implanted 0.5 mm above the PL-PFC viral injection spot (AP +2.9 mm, ML ±1.6 mm, DV -3.2 mm, with tips angled 17° toward the midline, fig. S1C). On the contralateral side of the optical fiber implant, after the electrodes were implanted, we added silicone artificial dura gel (Cambridge NeuroTech) to protect the dura. Vaseline was used to cover the movable parts of electrodes, including silicon probe shanks, flexible cables, and drive shuttles. Both optic fiber and drives were fixed to the skull screws with dental cement. After surgery, the rats were given a week of recovery time before neural recordings.

71

72

In vivo electrophysiological recordings and optogenetic stimulation

Before testing, animals with chronic optic fiber and electrode implants were given 30 minutes to adapt to the recording chamber on a mesh or glass table. Silicon probes were connected to a motorized commutator (OPT/Carousel M Commutator 2LED-4DHST-TH, Plexon) through 32-channel digital headstages (HST/32D, Plexon). The other end of the commutator was connected to the data acquisition system (Plexon). The optic fiber cannula was connected with a 465 nm blue light-emitting diode (LED) (OPT/LED_Blue_Compact_LC_magnetic, Plexon) through a mating sleeve (ADAF2, Thorlabs) and a fiber patch cable. The blue LED was mounted on the same carousel commutator by a magnet.

Raw electrophysiological signals were recorded at 40 kHz through a 64-channel OmniPlex data acquisition system (Plexon). Additionally, the event time stamps, including pain stimulus events, pain onset detection events, and optogenetic stimulus events, were recorded through PlexControl (Plexon) for further offline data analysis.

For optogenetic stimulation, we used OmniPlex digital 5V output to control the blue LED. The output power of the optic fiber tip was calibrated before the experiments. The parameters for optogenetic stimulation were 20 Hz with 10-ms pulse width and a duration of 5 s (33).

During the recording, two cameras (DMK23U, Imaging Source; FDR-AX53, Sony) were used to record both the behavior of the rats and the online-decoding results of the BMI client software. At the beginning of each recording session, the cameras were synchronized with the neural recording by sending a signal marker. Long inter-trial intervals were used between trials to avoid behavioral or neural sensitization.

Prelimbic PFC stimulating electrode and silicon probe implantation surgery

Two 32-channel silicon probes (Buzsaki32-H32, NeuroNexus Technologies, or ASSY-116 E-1, Cambridge NeuroTech) were implanted as described above to record LFPs from the rat S1 and ACC. A twisted pair wire stimulating electrode (California Fine Wire Co., M259400) was implanted at the PL-PFC (AP +2.9 mm, ML ±1.6 mm, DV -3.7 mm, with tips angled 17° toward the midline, fig. S1D). The stimulating electrode and silicon probe drives were fixed to the skull screws with dental cement. After surgery, rats were given a week of recovery time before neural recordings.

Electrical deep brain stimulation (DBS)

For DBS, we used a World Precision Instruments A365 stimulus isolator to send a sequence of biphasic-square waves. The parameters for DBS were 20 Hz with 25 μ A current amplitude and 40% duty cycle, and the duration was 5 seconds (fig. S9).

Multi-region neural interface development

Our customized BMI software supported the hardware platform designed for online LFP decoding analysis and for providing a graphical user interface (GUI, fig. S2). Our software was run on a desktop PC (Intel Xeon E5-1620 CPU, 3.5 GHz, 48 GB memory, Window OS). The BMI system client software was used to manage the components and tasks, which includes the following modules: 1) configuration management, 2) data acquisition and buffering, 3) online training/decoding algorithms, 4) external device control, and 5) user interfaces. This software was developed using the C++ programming language with the software developing tool kit made by

Plexon and other open-source software packages. In order to provide maximum flexibility while minimizing the maintenance complexity, the functional modules in the software were designed with encapsulation for decoupling purpose. In the GUI, users had the ability to select and change the LFP channels, and select the pain detection algorithm based on single or multiple brain regions.

Event-related potential (ERP) analysis

Event-related potentials (ERPs) are also referred to as "evoked potentials" when occurring soon after a stimulus. A cortical ERP reflects the coordinated behavior of a large number of neurons in relation to an external or internal event. Traditional ERP analysis is based on trial averaging, but we reported the ERP statistics here based on single-trial analyses. From LFP recordings, we identified the induced ERPs within a 5-s window after the stimulus onset (42). To account for signal variability across channels, we averaged the LFP signals across channels from one cortical area. We identified the peak of the ERP and defined the latency as the time between the stimulus onset and the ERP peak.

LFP power spectrum analysis

In single-trial analyses, we computed the power spectrogram in the time-frequency representation by using a moving window. Multi-tapered spectral analyses for LFP spectrogram were performed using the Chronux toolbox(70) (chronux.org). Specifically, we chose a half-bandwidth parameter W such that the windowing functions were maximally concentrated within [-W, W]. We chose W > 1/T (where T denotes the duration) such that the Slepian taper functions were well concentrated in frequency and had bias reducing characteristics. We used the tapers setup [TW, N] for the Chronux function setup, where TW is the time-bandwidth product, and $N = 2 \times TW - 1$ is

the number of tapers. Since the taper functions are mutually orthogonal, they give independent spectral estimates. We used a moving window length of 0.5 s and a step size of 50 ms. We used TW = 5 for the LFP spectrogram. From the LFP spectrogram, we computed the Z-scored spectrogram, where the baseline mean was subtracted from the energy at each frequency (i.e., the row of the heatmap) and normalized by the baseline standard deviation at each frequency. The baseline was defined as the 5-s period before the stimulus presentation.

Unsupervised machine learning analysis for detecting the onset of pain signals

For the LFP features, we used band-pass filtering to extract band-limited signals (Fig. 1C) and computed the band-limited LFP power at the low gamma (30-50 Hz), high gamma (50-100 Hz) and ultra-high frequency ranges (300-500 Hz). The >300 Hz frequency range is also known as the spiking-band power or multiunit activity(60). The features were averaged by time (within a bin size) to generate a three-dimensional time series for a single selected LFP channel. In practice, we selected one channel from the ACC and one channel from the S1. The criteria of channel selection depended on the artifact, signal-to-noise ratio (SNR), or the spiking activity.

We used an unsupervised machine learning method to detect the onset of pain. We developed this decoding strategy based on a state space model (SSM; Fig. 1D) or linear dynamical system (LDS). The SSM consists of a state equation and a measurement equation. In the state equation, we assumed that the ACC or S1 LFP-derived spectrotemporal features (i.e., amplitude of the bandpass filtered signals at 30-50 Hz, 50-100 Hz, and 300-500 Hz) at the k-th time index (bin size: 100 ms), represented by a vector \mathbf{y}_k , was driven by a univariate latent Markovian process z_k :

$$z_k = az_{k-1} + \epsilon_k$$

where ϵ_k specifies a temporal Gaussian prior (with zero mean and variance σ^2) on the latent process, and 0 < |a| < 1 denotes the first-order autoregressive (AR) coefficient.

167

In the measurement equation, we assumed that the measurement y_k was drawn from a linear

169 Gaussian system

$$y_k = cz_k + d + v$$

where d denotes a constant; c denotes the modulation coefficient; and v denotes the uncorrelated Gaussian noise with zero mean and covariance matrix Σ . The latent variable z_k was viewed as a common input that drives the pain responses in the measurement y_k .

174

175

176

177

178

179

186

187

We let Θ denote all unknown model parameters, and we have developed an iterative expectation-maximization (EM) algorithm to estimate latent states $\{z_k\}$ (E-step) and unknown parameters $\Theta = \{a, c, d, \sigma^2, \Sigma\}$ (M-step). Details of this estimation procedure have been reported previously (38). In an online filtering operation, we used a Kalman filter to estimate the predicted latent state. The Kalman filter equations are given as follows (71):

$$\hat{z}_{k|k-1} = a\hat{z}_{k-1|k-1}$$

$$Q_{k|k-1} = a^2 Q_{k-1|k-1} + \sigma^2$$

$$\widehat{\mathbf{y}}_{k|k-1} = \mathbf{c}\widehat{\mathbf{z}}_{k|k-1} + \mathbf{d}$$

$$G_k = Q_{k|k-1}c^T(Q_{k|k-1}cc^T + \Sigma)^{-1}$$

184
$$\hat{z}_{k|k} = \hat{z}_{k|k-1} + G_k(y_k - \hat{y}_{k|k-1})$$

$$Q_{k|k} = Q_{k|k-1}(1 - G_k c)$$

where the subscripts k|k-1 and k|k denote the estimates from the prediction and filtering operations, respectively. G_k denotes the Kalman gain; $\hat{z}_{k|k}$ and $Q_{k|k}$ denote the posterior mean and variance

of the latent state, respectively. Together, the recursive updates between prediction and filtering equations produced a sequential Bayesian estimate of the latent state $\hat{z}_{k|k}$. We further computed the Z-score of the state estimate related to the baseline: $Z_{score} = \frac{z-\text{mean}(z_{\text{baseline}})}{\text{SD}(z_{\text{baseline}})}$. In the training trial for model identification, the baseline was defined by the pre-stimulus 5-s period before the noxious stimulus onset. We monitored the time-varying Z-score to assess the significance of change point detection (Fig. 1E). The significance criterion of Z-score change was determined by a critical threshold. Using a 95% confidence interval, we detected a change when the lower bound of the Z-score was greater than 3.38 (i.e., Z-score-CI > 3.38) or the upper bound of Z-score was less than -3.38 (i.e., Z-score + CI < -3.38), where the confidence interval (CI) at each time point was derived from the state posterior variance $Q_{k|k}$.

After independently deriving the Z-scores $\{Z_k^{ACC}\}$ and $\{Z_k^{S1}\}$ from the ACC and S1 LFP-derived features, respectively, we computed a moving-average cross-correlation function (CCF) between two Z-score traces (42)

 $CCF_k = (1 - \rho)CCF_{k-1} + \rho(Z_k^{ACC})^m (Z_k^{S1})^n$

where $0 < \rho < 1$ is a forgetting factor, $0.5 \le m$, $n \le 1$ are the scaling exponents (default value: 0.5). The smaller the forgetting factor ρ , the smoother the CCF curve. A smaller exponent value would magnify the impact of a Z-score smaller than 1, while reducing the impact of a higher Z-score. When two Z-score traces followed a consistent trend, the CCF increased in absolute value; otherwise, it remained at the baseline. Furthermore, we computed the Z-score of CCF relative to the same baseline. We tracked the CCF area above the threefold standard deviation (SD) of baseline statistics. The area value would accumulate when the CCF was above the threshold, and

reset to 0 when the CCF was below the threshold. We declared the change point – pain onset – when the accumulated area value exceeded a predefined threshold.

Area under curve (AUC) analysis

The ROC (receiver operating characteristic) curve is derived from a series of different binary classification methods (cutoff value or decision threshold), with the true positive rate (sensitivity) as the y-axis, and the false positive rate (1 - specificity) as the x-axis. AUC is defined as the area under the ROC curve and the coordinate axis. The value of this area cannot be greater than 1. The closer the AUC is to 1.0, the higher the authenticity of the detection method; when it is close to 0.5, the authenticity is the lowest and it indicates a chance accuracy.

Complete Freund's Adjuvant (CFA) administration

To induce chronic inflammatory pain, 0.1 mL of CFA (*Mycobacterium tuberculosis*, Sigma-Aldrich) was suspended in a 1:1 oil saline emulsion and injected subcutaneously into the hind paw contralateral to the implanted recording electrodes.

Spared Nerve Injury (SNI) Surgery

As shown in previous studies(58), under anesthesia (isoflurane 2%), the lateral left thigh of the rat was incised, and the biceps femoris muscle was exposed to identify the sciatic nerve and its three distal branches (the common peroneal, tibial, and sural nerves, respectively). The common peroneal and tibial nerves were each tied off with nonabsorbent 5-0 silk sutures and transected. To avoid subsequent nerve regeneration, an additional 5mm of nerve distal to the point of transection were further resected. The sural nerve was left intact, to produce a state of increased sensitivity

and hyperalgesia in the ipsilateral hind paw. The biceps femoris muscle was then closed with 4-0 absorbable sutures and the skin incision was closed by surgical staples.

Hargreaves test (Plantar test)

The Hargreaves test was performed to observe the response of rats to acute thermal stimulation. We used a movable radiant heat-emitting device with an aperture of 10 mm (37370 plantar test, Ugo Basile) to provide acute thermal stimulation to the plantar aspect of the hind paw. The rats were placed in a plexiglass chamber on a Hargreaves glass table. After a period of adaptation to this set up, an IR intensity of 70 was used to provide noxious thermal stimulation; alternatively, as a control, an IR intensity of 10 was used to produce non-noxious thermal stimulation. IR stimuli were terminated by paw withdrawals or kept for a duration of 30 s. We conducted at least 5 trials to measure the paw withdrawal latency for each testing condition. The inter-trial interval was approximately 5 minutes. The paw withdrawal latency was automatically recorded.

For online BMI experiments, 1-3 noxious stimulus tests ("calibration trials") were first performed on the SSM decoder to train the SSM model parameters.

Mechanical allodynia test

A Dixon up-down method with von Frey (vF) filaments was used to assess mechanical allodynia(58). Rats were placed in a plexiglass container over a mesh table and acclimated for 20 minutes. 1-5 trials of the 6g vF stimulus was delivered to the hind paw of the rat to train the SSM. Subsequently the rats were allowed a period of rest to avoid hypersensitivity. A set with logarithmically incremental stiffness were then applied to the hind paw in order to calculate 50%

withdrawal thresholds. vF filaments were applied to the plantar surface of the hind paw contralateral to the brain recording site.

Conditioned place preference (CPP) test for evoked pain in naïve and CFA-treated rats

CPP experiments were performed in a connected two-chamber device. A high-speed camera (Computar CS-Mount 2.8-12mm Varifocal Lens) was used to record a top-down view of animal movements in each chamber. Results were analyzed by the AnyMaze software (Stoelting Co.). Afterwards an independent experimenter visually verified these results by viewing the recorded video. The CPP protocol included preconditioning (baseline), conditioning, and testing phases. During 10-min preconditioning, the rat moved freely between the two chambers, and AnyMaze measured the time spent in each chamber. If the rats spent more than 500 s or less than 100 s in either chamber during the preconditioning phase, these results were not used in further testing. After decoder training, the rat was then conditioned with a different treatment in each chamber.

During the conditioning phase, the animal was confined to one of the chambers. In both chambers, rats received peripheral stimulus. One of the chambers was paired with a treatment condition and the other chamber was paired with a control condition. Controls would be either no optogenetic stimulation, manually controlled stimulation (light was turned on by the experimenter prior to peripheral stimulations), or random optogenetic stimulation of matching intensity and duration. Treatment and control chamber pairings were counterbalanced. In naive rats, we used pin prick (PP) and 6g vF as noxious and non-noxious stimuli, respectively. In CFA rats, 6g vF (noxious) and 0.4g vF (non-noxious) were used to deliver peripheral stimulus to the hind paw, and the 6g vF stimulus was used to train the model.

Finally, during the 10-min testing phase, the animal could move freely between the chambers without any external peripheral or optogenetic stimulations. We used the AnyMaze software to analyze the time the rats spent in each chamber at each phase to calculate the CPP score. The CPP score was defined by the difference in the time the rats spent in the chamber associated with the treatment condition between the testing and preconditioning phases.

CPP test for spontaneous or tonic pain in CFA-treated rats

To assess spontaneous or tonic pain induced by CFA, we adapted a traditional CPP assay (37, 44). The preconditioning and testing phase still lasted for 10 minutes, but the conditioning phase was prolonged to 60 minutes. During this conditioning phase, no peripheral stimulus was given. One of the chambers was paired with BMI-triggered optogenetic activation of the PL-PFC, whereas the other chamber was paired with the control condition (either randomly delivered optogenetic activations of matching duration and intensity or no optogenetic activation). Treatment and control chamber pairings were counterbalanced. During the testing phase (10 minutes), the rats were allowed to move freely.

For all behavioral tests, the experimenter is blinded to the treatment condition of the animal.

Immunohistochemistry

Rats were deeply anesthetized with isoflurane and transcardially perfused with ice-cold phosphate buffer saline (PBS) followed by ice-cold 4% paraformaldehyde (PFA) in PBS. Brains were placed in PFA overnight to fix the tissue and then transferred to 30% sucrose in PBS for 3 days. Next, a

Leica CM3050S cryostat (Leica Biosystems) was used to collect 20 µm coronal sections. Images containing electrodes were stained with cresyl violet and viewed using an Axio Zoom widefield microscope (Carl Zeiss). Sections were also made after viral transfer for opsin verification.

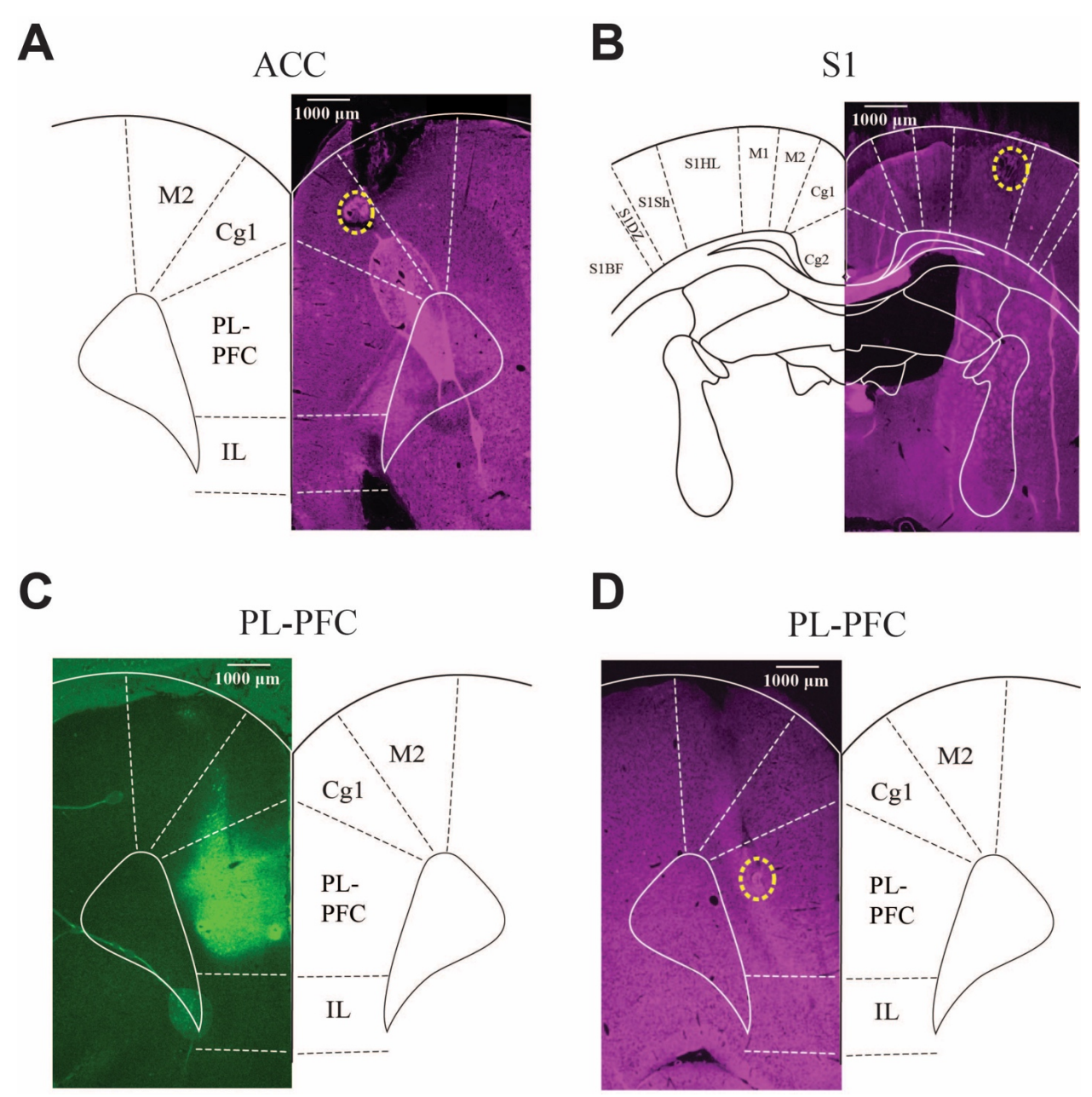
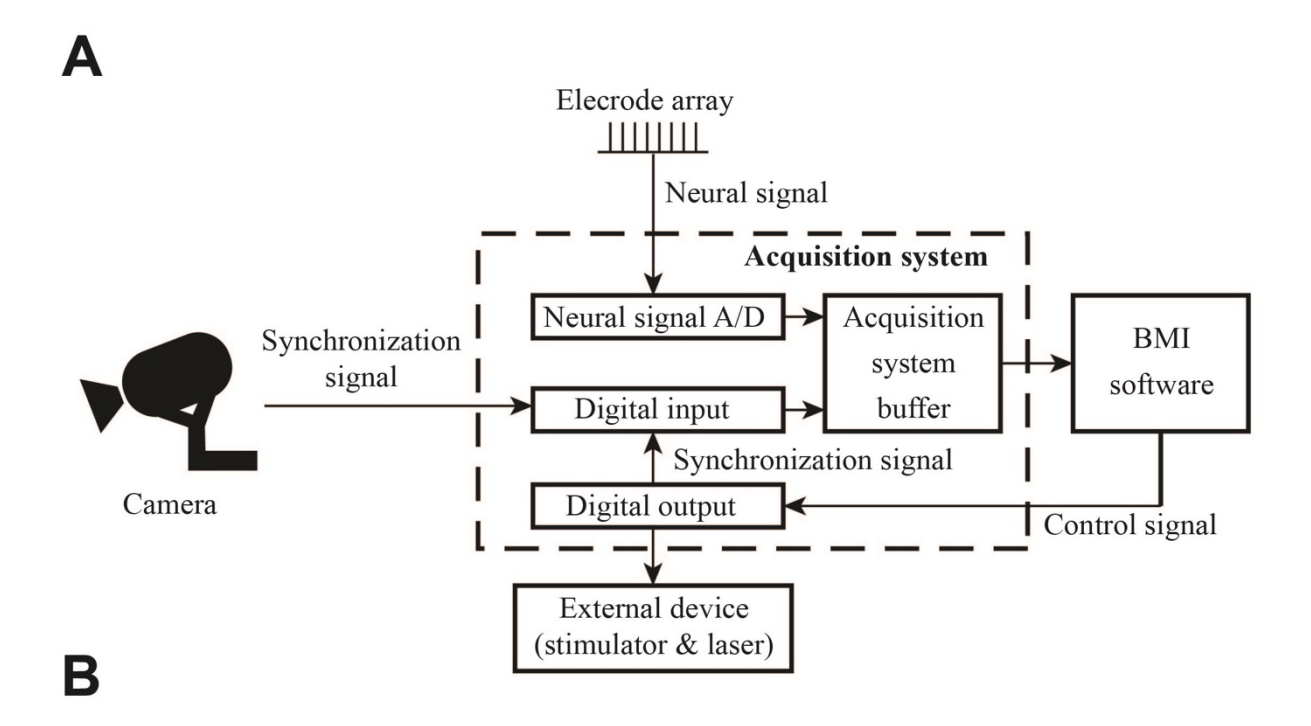


Fig. S1. Histology showing viral expression, and optic fiber and silicon probe implantations. (A) Histology showing the location of representative electrodes implanted in the rat ACC, marked by a yellow circle. (B) Histology showing the location of representative electrodes implanted in the rat S1 (hind paw region), marked by a yellow circle. (C) Channelrhodopsin (ChR2) is expressed selectively in the PL-PFC. (D) Histology showing the location of representative stimulating electrode implanted in the rat PL-PFC, marked by a yellow circle.



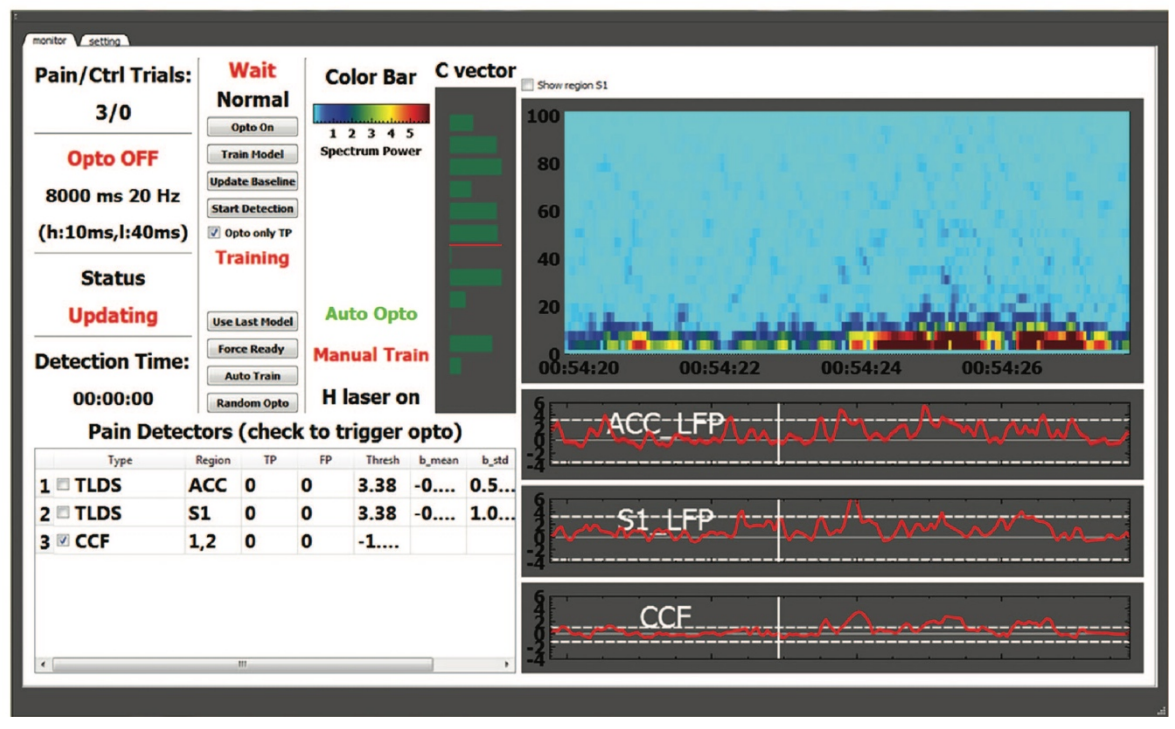
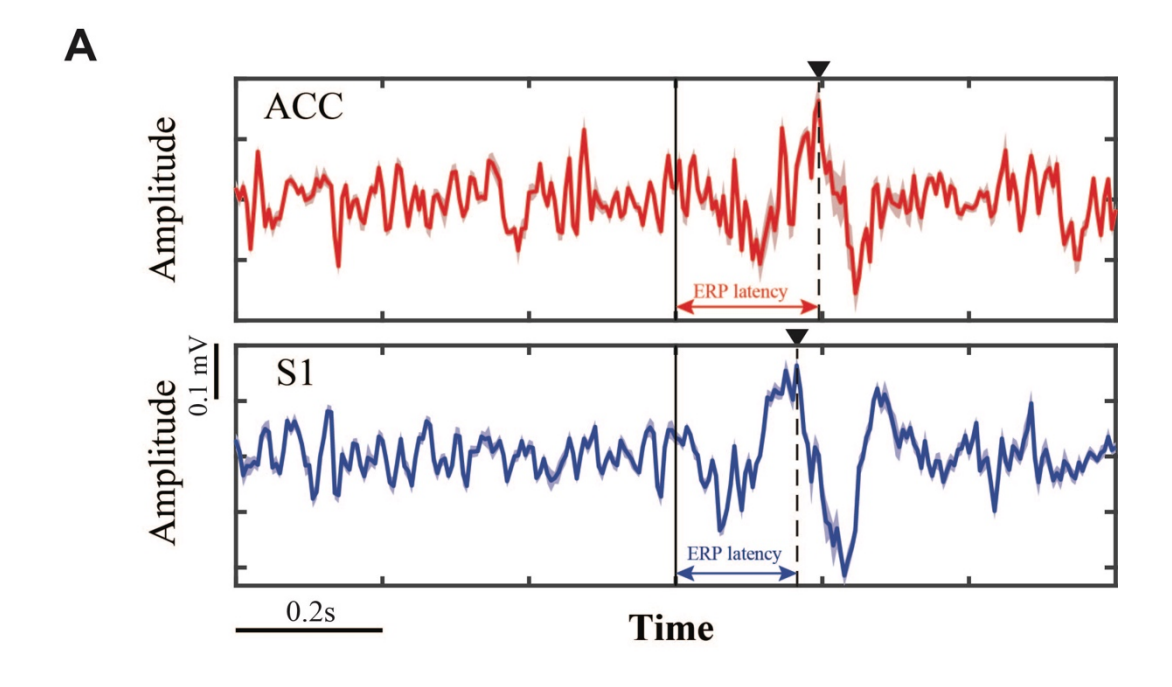


Fig. S2. Schematic of software design for a closed-loop multi-region LFP-based BMI. (A) Schematic of the brain machine interface (BMI). (B) Graphical user interface (GUI) of the BMI. Users can select the LFP channels and visualize LFP signals in real-time. Users have the option to select the detection strategy (based on the ACC, S1, or combination of both – the CCF method) and change the significance threshold criterion.



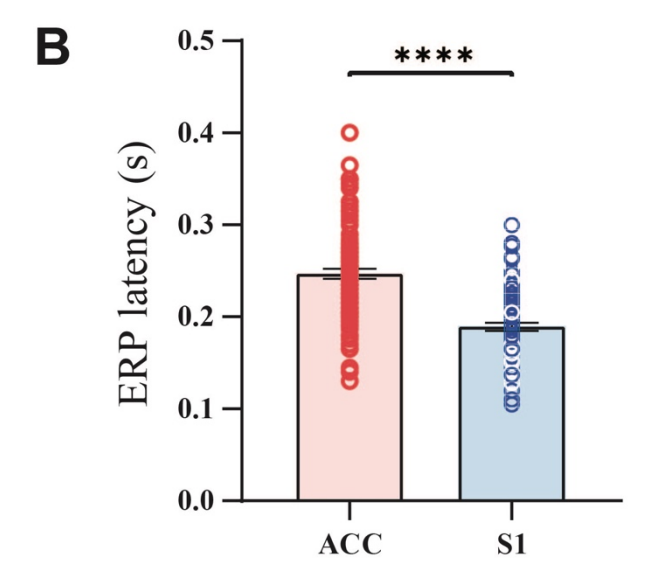
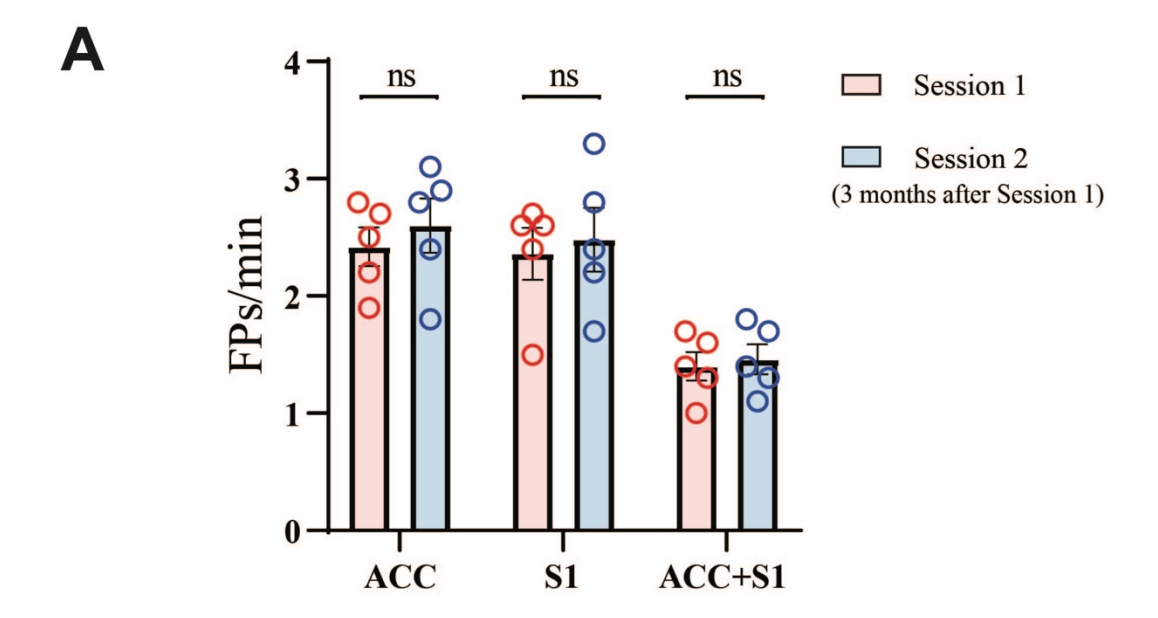


Fig. S3. Pain-evoked event-related potentials (ERPs) analysis. (A) Illustration of concurrent LFP signals in the ACC and S1. ERPs are marked by black triangles. Onset of a noxious stimulus (pin prick, PP) is marked by vertical line. The traces mark the signal-channel trace, which shows a large overlap with the channel-averaged trace (shaded area denotes SEM). The red trace indicates ACC's LFP signal and the blue trace indicates S1's LFP signal. The double arrows mark the ERP latency. (B) Comparison of ERP latency between the ACC and S1 (n = 96 trials from 5 rats). On average, the ERP latency in the S1 was shorter than that of the ACC (n = 96; ****P < 0.0001, paired t-test).



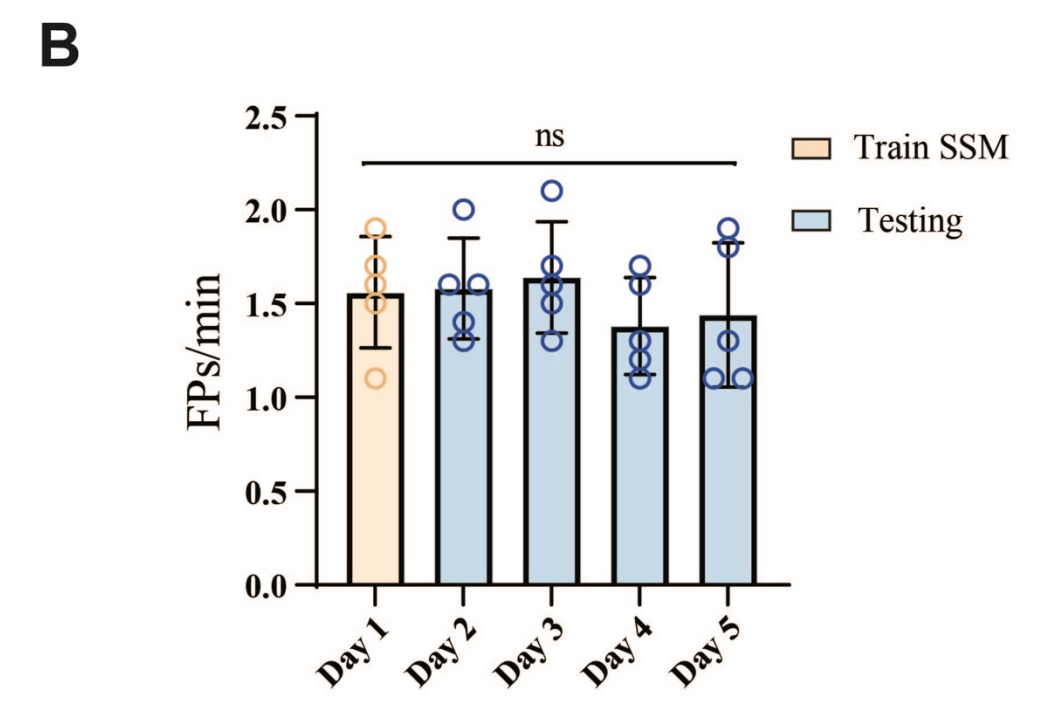


Fig. S4. False detection rate in cross session analysis. (A) Comparison of false detection rate based on LFP decoding strategies using the ACC, S1 and combined (ACC + S1) signals in Session 1 and Session 2, n = 5; P = 0.6183 (ACC), P = 0.7292 (S1), P = 0.8133 (ACC+S1), paired t-test. (B) Comparison of FP detection rates based on model parameters set 5 days apart. We used the first 3 trials on Day 1 to train the parameters of SSM, and then used these same parameters to detect pain on the subsequent 5 days. n = 5; P = 0.6888, one-way ANOVA with repeated measures and post-hoc Tukey's multiple comparison tests.

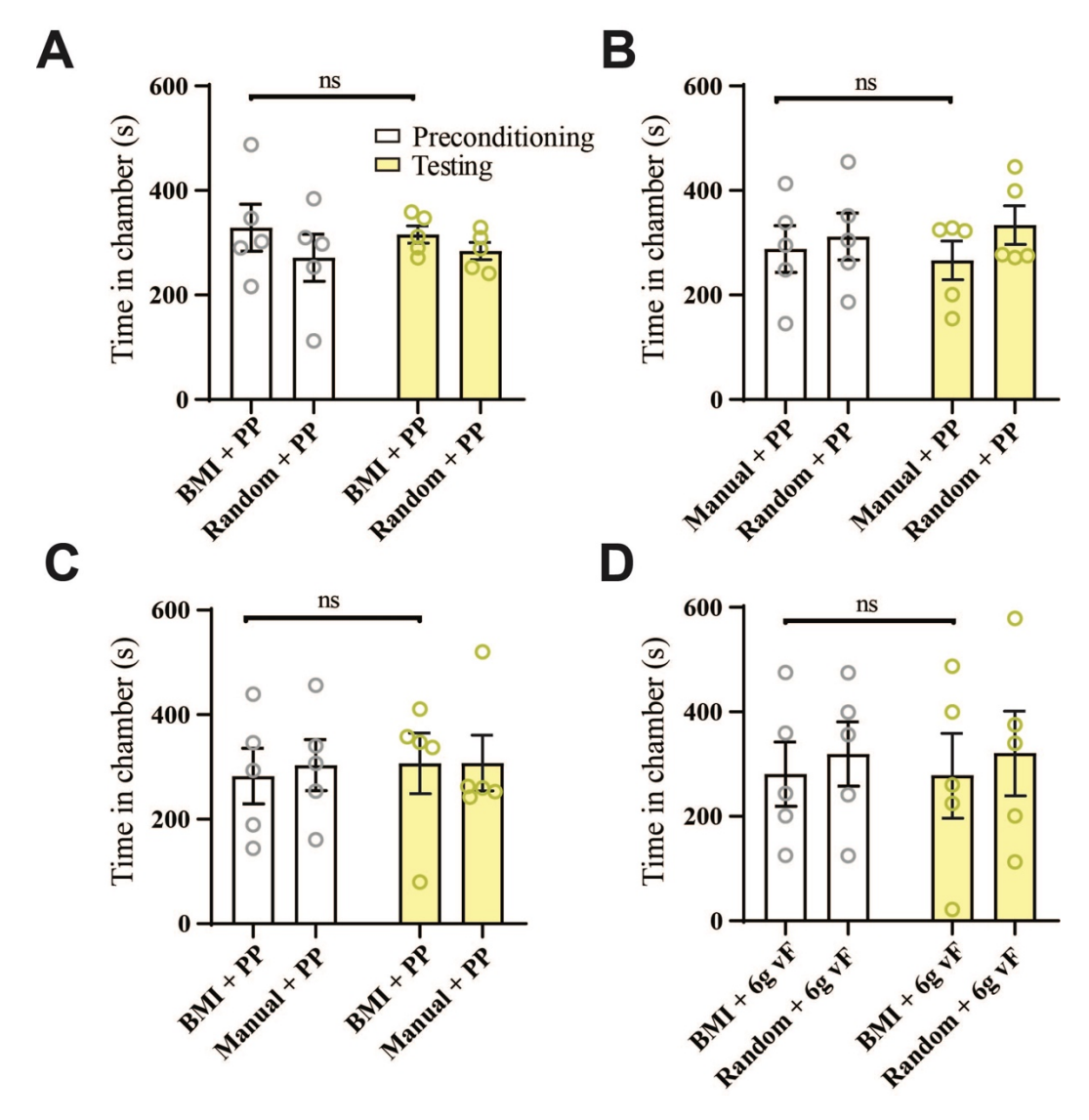


Fig. S5. LFP-based BMI does not alter pain-aversive behaviors in YFP-treated (control) rats.

(A) In the conditioned place preference (CPP) assay, during conditioning, one of the chambers was paired with BMI and PP, whereas the opposite chamber was paired with random PL-PFC light treatment of matching duration and intensity and PP. After conditioning, rats expressing YFP showed no preference for either chamber. n = 5; P = 0.988, paired t-test. (B) After conditioning, YFP rats showed no preference for either manually controlled light treatment or randomly delivered light treatment in the presence of PP. n = 5; P = 0.34, paired t-test. (C) After conditioning, YFP rats showed no preference for either BMI controlled light treatment or manually controlled light treatment in the presence of PP. n = 5; P = 0.915, paired t-test. (D) After conditioning, YFP rats showed no preference for either BMI controlled light treatment or randomly delivered light treatment in the presence of non-noxious 6g vF stimuli. n = 5; P = 0.945, paired t-test.

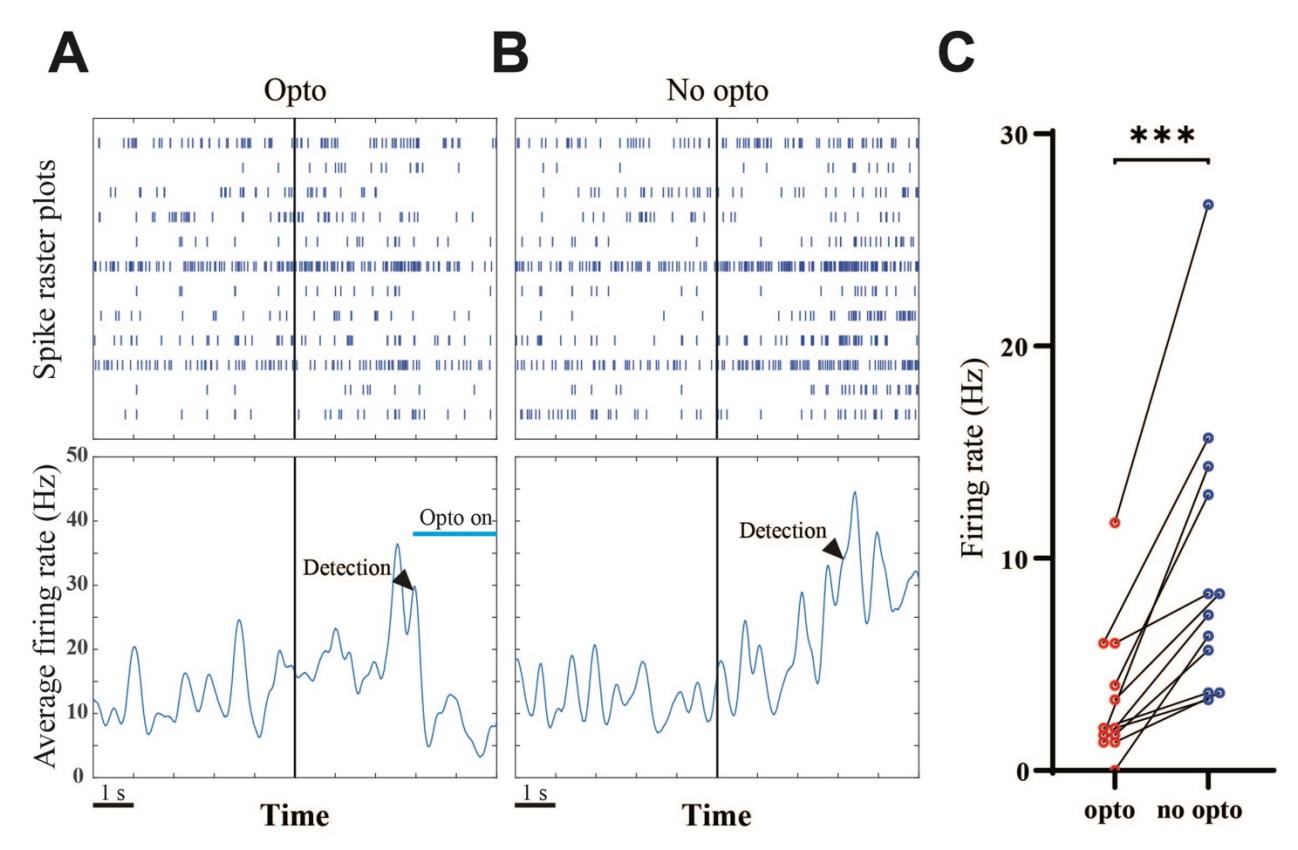
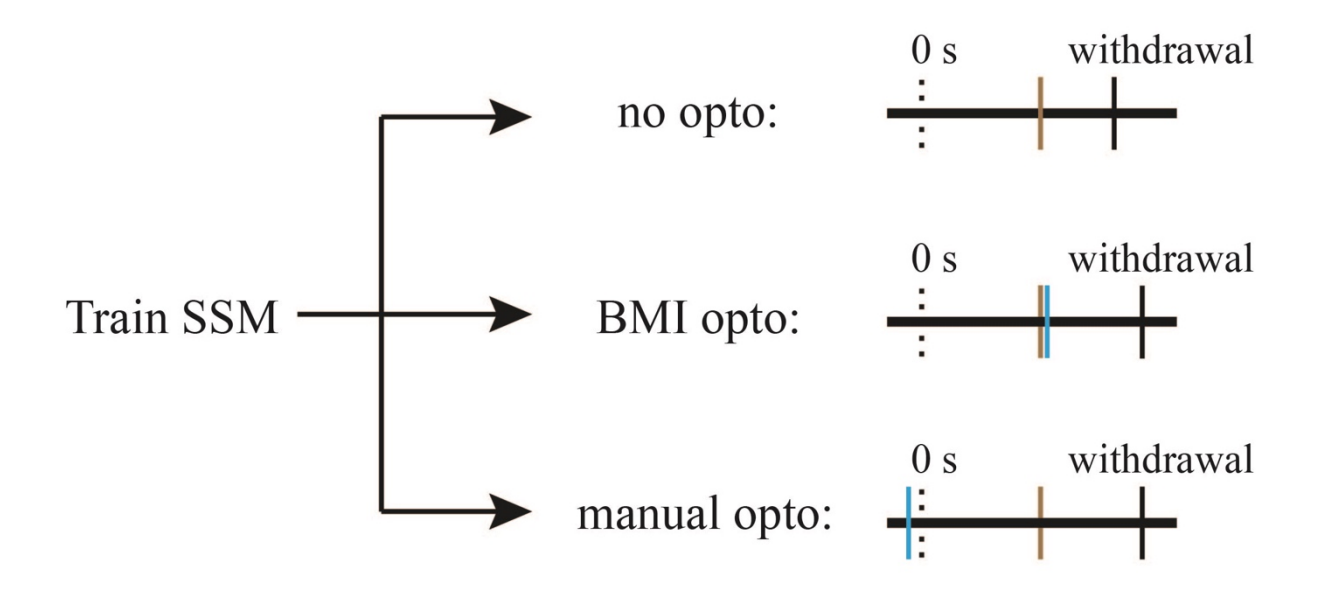


Fig. S6. BMI treatment reduces the neural response to thermal noxious stimuli. (A) An example session showing neural spikes in the ACC in response to thermal stimuli during the Hargreaves' test with BMI implementation. The top panel shows the Raster plots of pain-responsive neurons in the ACC, and the bottom panel shows the average firing rate (Z-score) of these neurons. The vertical solid line indicates the onset of a noxious thermal stimulus (IR 70). The bold triangle indicates the pain detection point, and the blue horizontal line shows optogenetic PL-PFC activation triggered by the BMI. (B) An example session showing neural spikes in the ACC in response to thermal stimuli during the Hargreaves' test without BMI implementation. (C) Compare the firing rate of 12 units within 3 seconds after detection under opto and no opto conditions. n = 12 units; ***P = 0.0005, paired t-test.

Pain detection Opto stimulation Stimulus onset Withdrawal



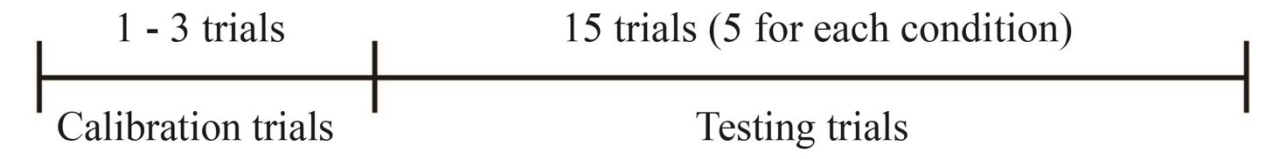


Fig. S7. Schematic of acute thermal pain assays. First, 1-3 noxious stimulation trials ("calibration trials") - when a noxious thermal stimulus (IR 70) is applied to the paws of a rat under the Hargreaves table - were performed to train the SSM model parameters. Next, 15 trials of three different testing conditions were applied randomly. The first condition was "no opto", where the system did not send any triggers for optogenetic stimulation during these trials. The second condition was "BMI opto", where the pain decoder in the BMI automatically turned on optogenetic stimulation of PL-PFC whenever a pain signal was detected. The time interval between detection and optogenetic stimulation onset was less than 1 ms. The third condition was "manual opto", where an experimenter manually turned on optogenetic stimulation right before the stimulus onset.

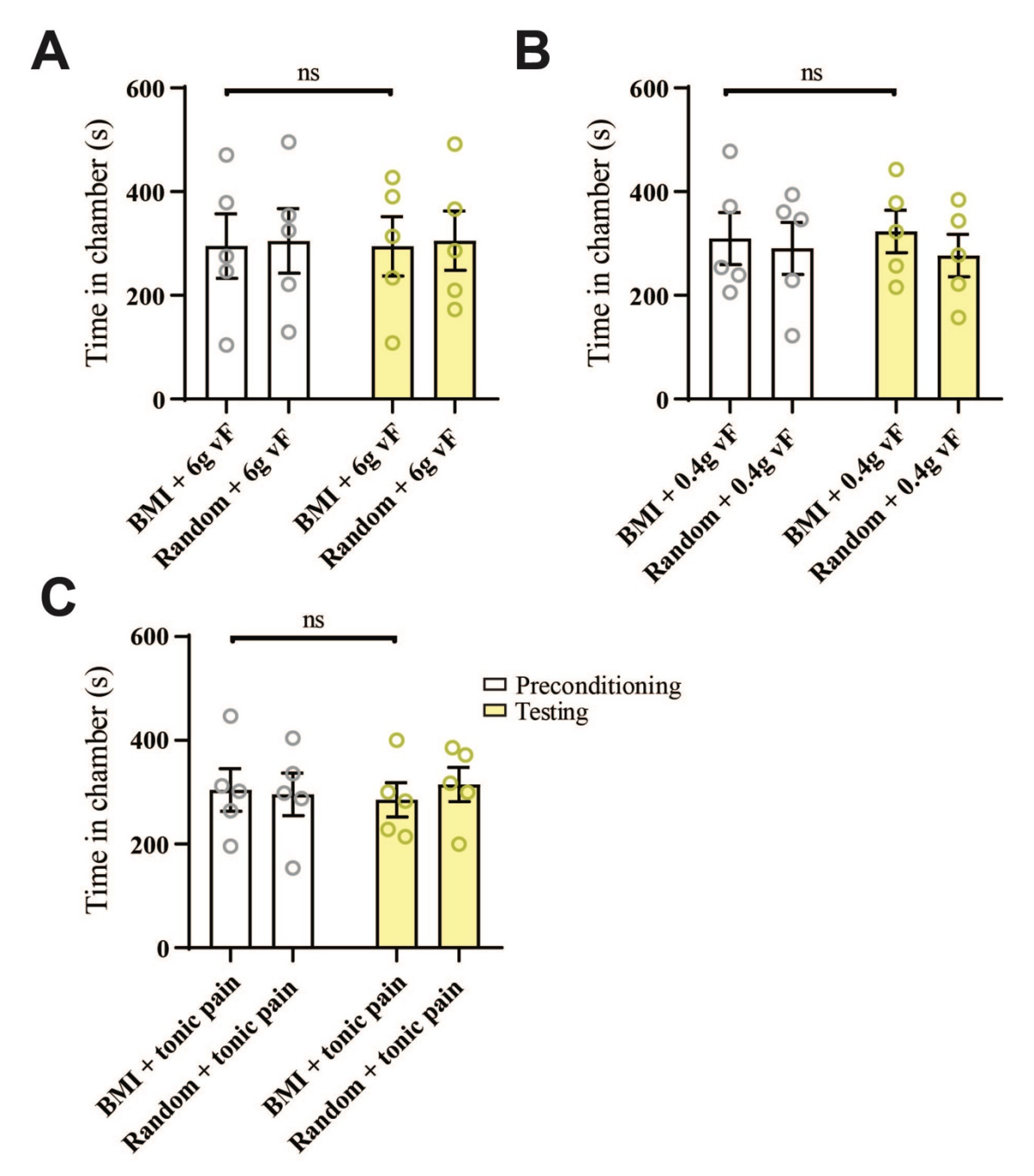


Fig. S8. CPP results of CFA-treated YFP (control) rats. (A) After conditioning, YFP rats showed no preference for either BMI-triggered light treatment or randomly delivered light treatment in the presence of noxious 6g vF stimuli. n = 5; P = 0.9876, paired t-test. (B) After conditioning, YFP rats showed no preference for either BMI or randomly delivered light treatment in the presence of non-noxious 0.4g vF stimuli. n = 5; P = 0.5363, paired t-test. (C) After conditioning, YFP rats showed no preference for either BMI or randomly delivered light treatment on the tonic CPP test. n = 5; P = 0.4313, paired t-test.

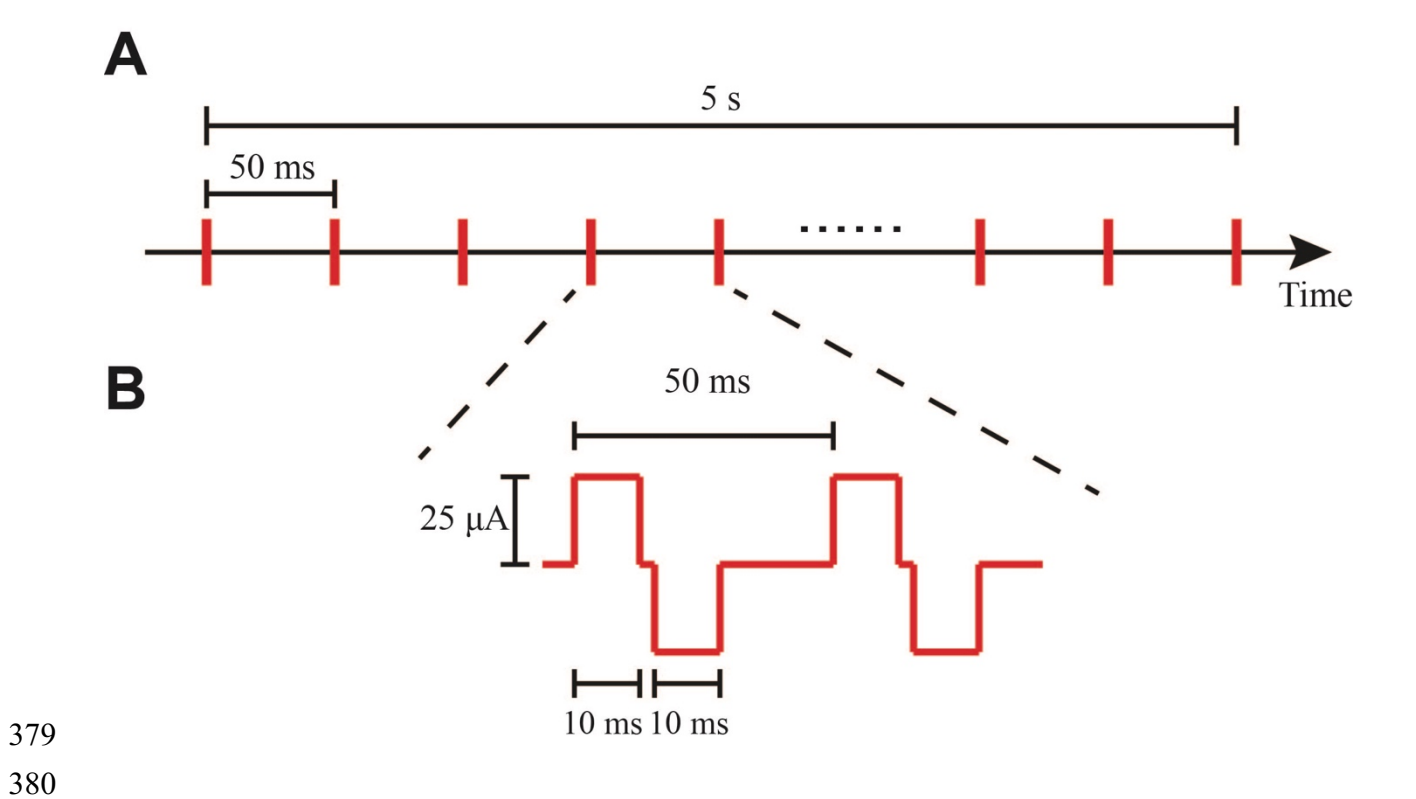


Fig. S9. Electrical deep brain stimulation (DBS) parameters. (A) The duration of each training trial of DBS was 5 s. DBS was delivered at a frequency of 20 Hz, with 25 μ A current amplitude and 40% duty cycle. (B) Parameters of the DBS waveform.

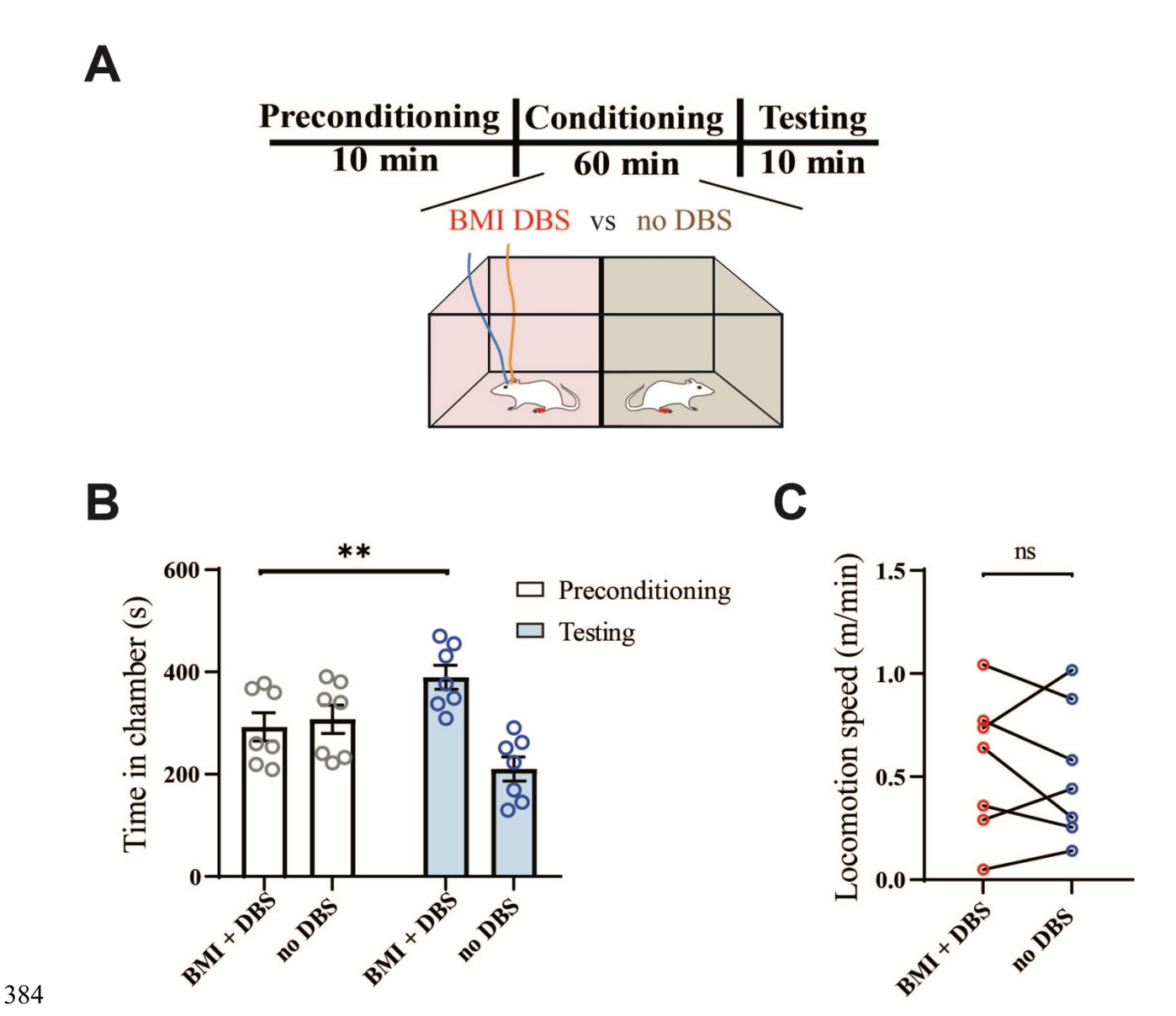


Fig. S10. The BMI-driven DBS provides specific treatment for CFA rats without obvious side effects. (A) Schematic of the CPP experiment to test tonic pain in CFA-treated rats. No peripheral stimuli were given. One chamber was paired with closed-loop BMI DBS, and the other chamber was paired with no DBS. (B) CFA-treated rats preferred the BMI chamber. n = 7; **P = 0.0052, paired t-test. (C) DBS produced no locomotion defects. n = 7; P = 0.647, paired t-test.

Table S1. Comparison of the area under curve (AUC) between various non-noxious and noxious acute mechanical stimulus based on different LFP decoding strategies

	ACC (mean ± s.e.m.)	S1 (mean ± s.e.m.)	CCF (mean ± s.e.m.)
2g vF (non-noxious)	0.505 ± 0.045	0.571 ± 0.048	0.542 ± 0.017
6g vF (non-noxious)	0.504 ± 0.025	0.554 ± 0.023	0.495 ± 0.038
Pin prick (noxious)	0.752 ± 0.022	0.754 ± 0.023	0.808 ± 0.019

	Acute Thermal Stimulus (mean ± s.e.m.)	Mechanical Stimulus in CFA Model (mean ± s.e.m.)	Mechanical Stimulus in SNI Model (mean ± s.e.m.)
non-noxious (IR 10 or 0.4g vF)	0.46 ± 0.027	0.518 ± 0.036	0.498 ± 0.047
noxious (IR 70 or 6g vF)	0.74 ± 0.030	0.776 ± 0.035	0.778 ± 0.032

Data file S1. Raw data. Provided as an Excel file.